CHALMERS
UNIVERSITY OF TECHNOLOGY

Multiscale Modelling of a Metallized Film Capacitor for HVDC Applications

Master's thesis in Electric Power Engineering

ANDREAS HJERT

Department of Materials and Manufacturing Technology
CHALMERS UNIVERSITY OF TECHNOLOGY
Gothenburg, Sweden 2017

Master's thesis 2017:203

Multiscale Modelling of a Metallized Film Capacitor for HVDC Applications

ANDREAS HJERT

Department of Materials and Manufacturing Technology
Division of High Voltage Engineering
Chalmers University of Technology
Gothenburg, Sweden 2017

Multiscale Modelling of a Metallized Film Capacitor for HVDC Applications
ANDREAS HJERT

Supervisor: Henric Malmkvist, Senior Engineer, ABB AB PPHV/TCCD
Examiner: Professor Yuriy Serdyuk, Chalmers University of Technology

Master's Thesis 2017:203
Department of Materials and Manufacturing Technology
Division of High Voltage Engineering
Chalmers University of Technology
SE-412 96 Gothenburg
Telephone +46 31 772 1000

Multiscale Modelling of a Metallized Film Capacitor for HVDC Applications
Andreas Hjert
Department of Materials and Manufacturing Technology
Chalmers University of Technology

Abstract

Metallized dielectric films used for high-voltage direct current (HVDC) Light capacitors are subjected to voltage ripples in operation. This leads to heat generation and a temperature rise in the capacitor. The operating temperature, which affects the function and the lifetime of the capacitor. Designs of capacitor units are evaluated by thermal stability tests to ensure thermal stability under overload conditions. It is therefore important for the designer to know locations of hot spots, the average temperature and the maximum temperature.

This thesis presents a multiphysics model of a HVDC Light capacitor unit simulating electric currents and heat transfer under the conditions of a thermal stability test. A capacitor unit consists of capacitor elements made of metallized films with large difference in scales. To overcome this, a multiscale approach have been used to model the capacitor unit. Effective properties and losses are computed on a small scale (several layers of metallized film) and utilized on a large scale (capacitor unit).

The performed calculations yield the impedance of the capacitor unit corresponding to the rated impedance with the effective properties implemented. The loss computed on the small scale is lower than average measured loss of a capacitor element. Additionally, the loss computed on the large scale matches the average measured loss of a capacitor unit. The hot spot of the capacitor unit is located at the front. The elements located there are hotter than the elements at the rear.

A multiscale modelling approach is utilized to model metallized film capacitors and to simulate thermal stability tests to estimate hot spots, average and maximum temperatures. The simulation results are compared to the results from a thermal stability test in a laboratory environment. This comparison shows that the simulated results are close to the test results. However, there are uncertainties related to heat transfer coefficients at different exterior boundaries of the unit and comparison with additional tests may improve the model.

Keywords: Metallized film capacitors, multiscale modelling, effective properties, electrical simulation, thermal simulation, HVDC, finite-element method.

Acknowledgements

Firstly, I would like to express my gratitude to my supervisor, Henric Malmkvist at ABB Capacitors for his guidance and valuable discussions during the thesis work. Secondly, I am deeply grateful to my examiner Professor Yuriy Serdyuk for his support and feedback.

This thesis was carried out during the spring term of 2017 at ABB Capacitors in Ludvika and I would like to thank the colleagues for their support and for making my stay in Ludvika pleasant. Finally, I would like to thank ABB Capacitors for giving me the chance to write this thesis.

Andreas Hjert, Gothenburg, June 2017

Contents

List of Figures

List of Tables

1

Introduction

Traditionally ABB Capacitors has used a trial and error approach when designing new capacitors. First, designs are estimated by simplified calculations, there-after tested in a laboratory environment and finally evaluated. Many mathematical and physical models are based on partial differential equations (PDEs). The possibility of finding solutions to PDEs by hand calculations are limited but computers offers an alternative by utilizing numerical methods. The design process could be improved by simulations in a finite element method (FEM) based program. Simulations can be used for estimations and the number of time consuming and expensive tests could be reduced [1]. This could also be beneficial in an environmental perspective if less prototypes are manufactured for testing purposes.

The capacitor of interest is utilized in high-voltage direct current (HVDC) Light applications. The technology is used to transmit electricity in the power range of 100 to 1200 MW over short and medium distances. The main benefit of HVDC transmission systems compared to high-voltage alternating current (HVAC) transmission systems, is increased transmission capacity of electrical power over longer distances with lower losses [2]. At present times when the transmission system is rapidly changing due to a growing demand of electricity and new climate change goals, HVDC Light has the ability to solve many of the problems that the system is facing. It enables connection of renewable energy sources like solar and hydro at remote locations, interconnection of AC grids for stabilization intentions and connection of offshore wind farms far out at sea. The core component of the technology is the power converter with insulated-gate bipolar transistors (IGBTs) as switches. The HVDC Light technology utilizes voltage source converters (VSC) for conversion between alternating current (AC) and direct current (DC) [3]. A core component of the converter is the capacitor (DryDCap) of dry type (no oil inside) consisting of many small modules (elements) each having a metallized film dielectric [4]. Traditional approaches for modelling of metallized film capacitors utilizes equivalent circuit approaches [5] [6] [7]. Computation of electrical lumped parameters (i.e resistances, capacitance and inductance) and modelling of elements have been extensively researched but future research are needed to model a unit of several elements. Furthermore, lifetime predictions are important for reliability and the temperature is then critical. Coupled electrical and thermal simulations could be used to estimate maximum and average temperatures of the capacitor and locate hot spots. A certain area of a capacitor unit may be hotter and it is important for the designer to know these spots since the aging of a capacitor is related to the temperature in the dielectric. When developing a new model it is important to validate the results from the simulations. In this thesis, a thermal stability test will be simulated and the proposed model will be evaluated against a test in a laboratory environment. To improve the design process of capacitors, research are need to develop a simulation model of a capacitor unit to locate hot spots and to compute average and maximum temperatures for lifetime estimations.

1.1 The Aim

To develop a couples electrical and thermal model of a capacitor unit for HVDC Light applications and simulate a thermal stability test to locate hot spots and to compute average and maximum temperatures.

1.2 Problem Description

The thesis includes the following key research points,

- A method for modelling metallized film dielectrics for electrical and thermal simulations and to compute dielectric losses.
- A model of a capacitor to simulate a thermal stability test to locate hot spots and to compute average and maximum temperatures.
- Validation of the results from the model against results from a thermal stability test in a laboratory environment and identify eventual deviations.

1.3 Scope

In this thesis, only capacitive field distribution will be considered. This is because a sinusoidal AC voltage is applied to the capacitor unit for the thermal stability test which is set to be simulated and hence only capacitive field distribution will be present. Additionally, only a fundamental frequency of 50 Hz is simulated as this is the test frequency of the applied voltage. The only temperature dependence of material properties considered is the electrical conductivity of copper for the busbar-system. Magnetic effects are out of the scope of the thesis and will not be considered. Furthermore, heat transfer is modelled by conduction and convection.

1.4 Thesis Outline

This thesis is divided into 5 chapters with several subsections. Chapter 2 describes the principle of HVDC Light capacitors and fundamentals of dielectrics. Chapter 3 presents the modelling procedure and the utilized software to model the capacitor. Furthermore, setups of different models, implemented boundary conditions, meshing and computation procedures of different properties are presented. Chapter 4 presents the results from the simulations and computed properties of interests.

Additionally, the results are discussed and comparison with measurements are presented. Chapter 5 includes conclusions of the thesis work and suggestions for future work.

1.5 Sustainable Perspective

One possible approach to the idea of sustainable development is to focus on human needs and human welfare. Then it is natural to focus on requirements to maintain and accomplish welfare in the present and also in the future. These requirements are often divided into ecological, economical and social dimensions. The dimensions can be thought of as means to accomplish the general goal of human welfare now and in the future. The ecological dimension includes preserving natural systems which provides humans with goods and services and thus the importance of sustaining the systems so future generations can have welfare as well as present generations. The second dimension, economical is related to managing resources. It is possible to divide resources into finite natural resources and manufactured capital. The finite resources are for example fossil fuels, metals and other resources that does not renew itself. The third and last dimension, social is related to the creation and preservation of institutions and structures which are important for the well-being of humans. Such institutions are for example, states, law institutions and international institutions as the United Nations[8].

It is difficult to argue that the development of a simulation model of a capacitor unit will affect social institutions and the sustainability of such institutions. But the two other dimensions could be used to analyze the sustainability of this thesis work. If a model is developed for electrical and thermal simulations, design ideas can be tested in a computer environment and provide estimations. This may lead to a reduction of the number of designs tested in a laboratory environment for the purpose of evaluation. To test a unit it is of course necessary to first construct the unit. If less designs are tested in a laboratory environment then less designs needs to be constructed. A prototype of a capacitor unit consist of a number of finite resources, like copper, aluminum and zinc. Furthermore, there is also a possibility to save energy since electrical energy is needed to perform tests. If less resources are needed in the development of a finalized design, less strain is put on the natural systems. This is related to the fact that mining and extracting metals from the crust of the earth affects the environment. Additionally, it will lead to less recycling and waste material since prototypes are often not used more than for evaluations. It is possible that simulation models like this one could help to create a more sustainable design process for capacitors by having less impact on the natural systems. Furthermore, it could improve the utilization of resources if the use of finite resources are reduced.

1.6 Ethics Perspective

The institute of electrical and electronics engineers (IEEE) code of ethics is a list of 10 points which the members commits to follow. The third point states that a member should be both honest and realistic when stating claims or making estimations based on available data [9]. This point is important when developing a simulation model and stating its use. A simulation model will always be an approximation of the real world and therefore it may have several limitations. It is then important to clearly state how the model is implemented and how results are obtained. Additionally, it is also important to clearly state the limitations of the model. For example what kind of physics are implemented and what is not considered. It also important to state if some effect is neglected or if some simplification have been made to develop the model. If this is followed, it will be easier for future users to evaluate the results and minimize the risk of misleading conclusions from the results.

2

Principles of HVDC Light Capacitors

In this chapter, HVDC Light, parallel-plate and metallized polymer film capacitors are introduced. Furthermore, the physics of dielectrics are described.

2.1 HVDC Light

The HVDC Light is the technology developed by ABB for high voltage direct current (HVDC) transmission which utilizes voltage source converters (VSCs). Traditionally the HVDC has been used to transmit high power and high currents. The introduction of HVDC Light has enable an economical transmission at lower current and power ratings. The converter topology is a cascaded two-level converter (CTL) which is a variant of VSCs. A simplified circuit diagram of one phase leg of a CTL can be seen in Figure 2.1. A phase leg consists of two arms, a positive (+DC) and a negative (-DC). The dotted lines between the two single valve cells are referring to the fact that there are several cascaded connections of single valve cells in one valve arm. As an example, 38 cells are connected per arm for a voltage level of 320 kV DC. A single valve cell is in fact a two-level converter and the name is referring to the fact that the output voltage can be switched between two discrete levels. The switches are insulated-gate bipolar transistors (IGBTs) which are controlled to produce a sinusoidal output voltage of a desired fundamental frequency. The parallel connection of an IGBT and a diode is called a valve. The valve cells in the figure can be switched in to three different states,

1. If T_1 is switched off and T_2 is switched on, the output voltage of the cell is equal to the capacitor voltage. In this state the capacitor is said to be inserted and will be charged or discharged depending on the direction of the current.
2. If instead T_1 is switched on and T_2 is switched off, the output voltage is equal to zero. In this state the capacitor is bypassed and its voltage remains constant (no charging or discharging).
3. If both of the IGBTs are switched off, the current can only be conducted by the diodes and the cell is said to be blocked.

The integrated capacitor is a core component in the CTL. It serves as an energy storage to enable control of the power flow. Since it is charged and discharged continuously during operation of the CTL, it is subjected to a fundamental component and ripple components of the current and hence losses occurs during operation[10]. In operation, the voltage across the capacitor is a DC voltage with a superimposed

AC voltage. This AC voltage is referred to as AC ripple. DryDCap is the product name of the DC capacitor developed by ABB for VSCs. The main difference compared to conventional capacitors are the filling material and the self-healing technology allowing higher stress levels. The electric stress level of the dielectric for dry capacitors is 225 $V/\mu m$, compared to 150 $V/\mu m$ for wet capacitors. This enables a high energy density for dry capacitors. Traditional capacitors are filled with oil but this capacitor is non-oil filled and there is no risk of leaks [4]. Important features of the DryDCap are presented in Table 2.1. The principles of the dielectric and self-healing will be described in section 2.3.

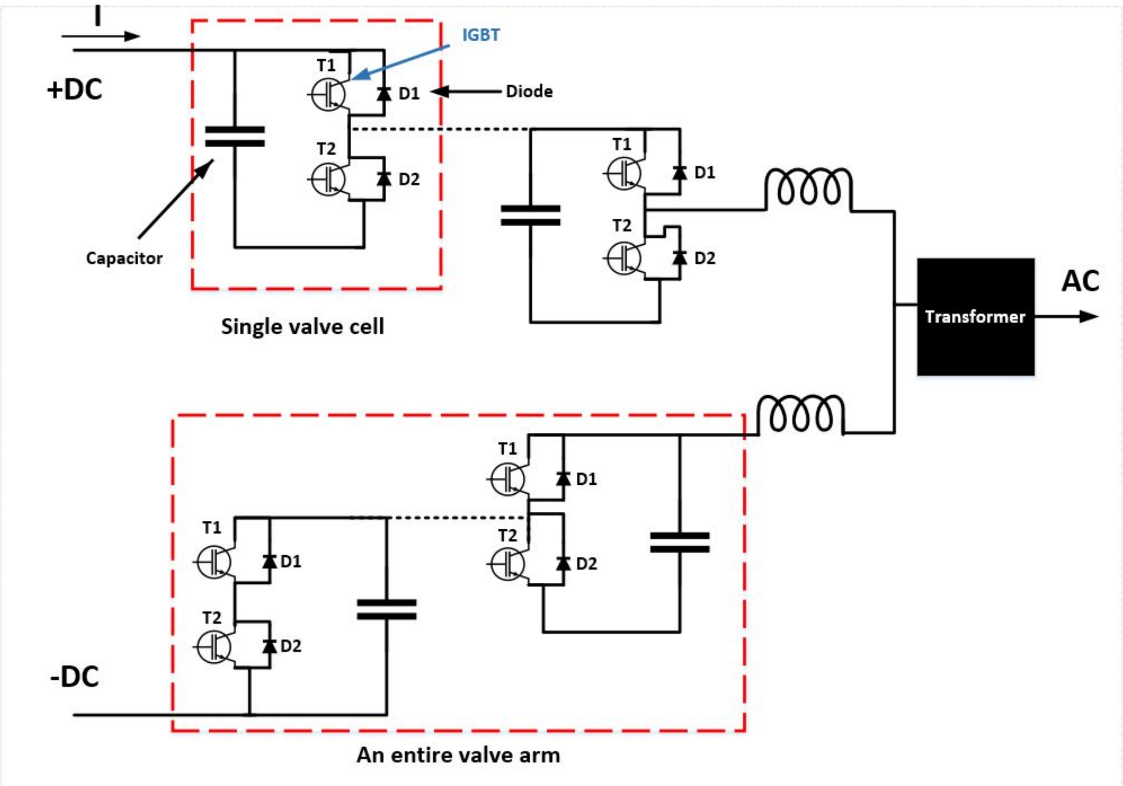

Figure 2.1: Illustration of a simplified circuit diagram of a cascaded two-level converter.

Table 2.1: Summary of key technical data of the DryDCap [4].

Technical data	
DC voltage	up to 4 kV
Current (rms)	up to 620 A
Capacitance	up to 10 mF
Operating temperature	+5 to +60 $°C$
Dielectric	Metallized Polypropylene film
Filling material	Polyurethane
Safety system	Self-healing

2.2 Fundamentals of Parallel-Plate Capacitors

In this section, the basics of parallel-plate capacitors, dielectrics in electric fields and the concept of complex permittivity are described.

2.2.1 Parallel-Plate Capacitor

A parallel-plate capacitor can be constructed by separating two metallic conductors and inserting an insulating material in between. This material is commonly referred to as dielectric. A typical arrangement is illustrated in Figure 2.2, where the direction of current (1) and the resulting electric field (2) are shown. Electrons will accumulate at the lower plate and thus it will become negatively charged. This will give rise to an electric field between the plates directed from positive towards negative. The charge build up will result in a voltage across the plates. The amount of charge is proportional to the voltage across the plates as

$$q = CU \tag{2.1}$$

where q is the total charge in C, C is the capacitance in F and U is the voltage in V. It can be observed that capacitance is a proportionality factor of the ration between stored charges and resulting voltage. The capacitance can be defined by geometrical properties as

$$C = \epsilon_0 \epsilon_r \frac{A}{d} \tag{2.2}$$

where ϵ_0 is the vacuum permittivity in F/m, ϵ_r is the relative permittivity of the dielectric material which is dimensionless, A is the plate area in m^2 and d is the distance between the plates in m.

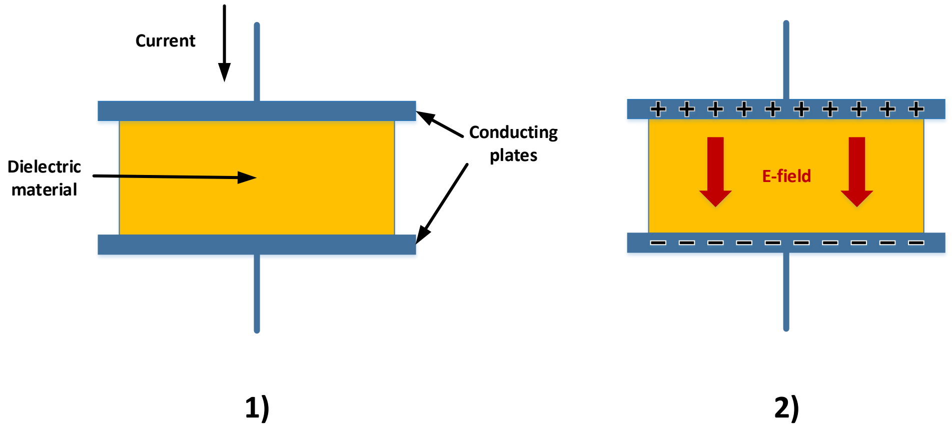

Figure 2.2: Illustration of a parallel-plate capacitor of two conductive plates separated by a dielectric (1) and accumulation of charges and the electric field (2).

As the voltage across the plates builds up, energy is delivered to the capacitor from the external circuit. The electric energy is stored in the electric field and given by

$$w_e(t) = \frac{1}{2}Cu(t)^2 \tag{2.3}$$

where $w_e(t)$ is the time instant electrical energy in J and $u(t)$ is the time-varying voltage across the plates in V [11]. If the voltage is sinusoidal, energy will be oscillating back and forth between the outer circuit and the capacitor, if $u(t) = U_0 sin(2\pi ft)$, Eq.2.3 becomes

$$w_e(t) = \frac{1}{2}C[U_0 sin(2\pi ft)]^2 = \frac{1}{4}CU_0^2[1 - cos(4\pi ft)] \tag{2.4}$$

where U_0 is the peak value, f is the frequency in Hz and t is the time in s. Since the energy is oscillating between 0 and a peak value($\frac{1}{2}CU_0^2$), it is common to compute the time average stored energy by integrating the energy over one period in the following way

$$We_{avg} = \frac{1}{4}CU_0^2\frac{1}{T}\int_0^T 1 - cos(4\pi ft)dt = \frac{1}{4}CU_0^2 \tag{2.5}$$

where T is one time period equal to $1/f$ in s. Eq.2.5 can be rearranged to compute the capacitance as follows

$$C = \frac{4We_{avg}}{U_0^2} \tag{2.6}$$

2.2.2 PDEs describing Electric Fields and Current Densities

There are three important equations when studying the interaction between electric charges and currents. Gauss's law (Eq.2.7) in free space describing the relationship between the divergence of the electric field and the charge density, Ohm's law (Eq.2.8) stating that the current density is proportional to the electric field by a factor and the continuity equation (Eq.2.9). The equations are stated as follows

$$\nabla \cdot \mathbf{E} = \frac{\rho}{\epsilon_0} \tag{2.7}$$

$$\mathbf{J} = \sigma \mathbf{E} \tag{2.8}$$

$$\nabla \cdot \mathbf{J} = -\frac{d\rho}{dt} \tag{2.9}$$

where $\mathbf{E}$ is the electric field vector in V/m, ρ is the total charge density in C/m^3, ϵ_0 is the permittivity of free space $8,85 \cdot 10^{-12}$ in F/m, $\mathbf{J}$ is the electric current density vector in A/m^2 and σ is a proportionality factor called conductivity of a medium in S/m [12]. In computational electromagnetics it is of interest to compute the electric field and the current density. The electric field can easily be obtained if the potential is known since the electric field is the gradient of a scalar potential given as

$$\mathbf{E} = -\nabla \varphi \tag{2.10}$$

where φ is the electric potential in V. By combining Eq.(2.7) and Eq.(2.10), Poisson's can be derived as follows

$$\nabla^2 \varphi = -\frac{\rho}{\epsilon_0} \tag{2.11}$$

In regions where there is no charge ($\rho = 0$), Eq.(2.11) reduces to Laplace's equation

$$\nabla^2 \varphi = 0 \tag{2.12}$$

If the potential distribution can be computed then the electric field and the current density can be obtained by Eq.(2.10) and Eq.(2.8) [12].

2.2.3 Dielectrics in Electric Fields

If a dielectric is placed in an electric field, charges can be displaced from their original positions. This give rise to induced dipole moments causing the dipoles to align in the same direction as the field. There are different types of polarization, namely atomic, electronic, dipolar (orientational) and interfacial polarization. These mechanisms give rise to accumulations of charge within the material described by a volume charge density as

$$\nabla \cdot \mathbf{P} = -\rho_b \tag{2.13}$$

where $\mathbf{P}$ is the polarization vector in C/m^2 and ρ_b is the bound charge density in C/m^3. Here bound charges are referring to charges displaced by the electric field but which are not moving freely through the material. This effect gives rise to the alternative form of Gauss's law in the presence of dielectrics,

$$\nabla \cdot \mathbf{D} = \rho_f \tag{2.14}$$

where $\mathbf{D}$ is the electric displacement vector in C/m^2 and ρ_f is the free charge density in C/m^3. It should be highlighted that this version of Gauss's law only depends on the free charge density. The electric displacement is given by the following relationship

$$\mathbf{D} = \epsilon_0 \mathbf{E} + \mathbf{P} \tag{2.15}$$

The relationship between $\mathbf{E}$ and $\mathbf{D}$ in linear dielectrics is given by a proportionality constant and can be expressed as

$$\mathbf{D} = \epsilon_0 \epsilon_r \mathbf{E} \tag{2.16}$$

where ϵ_r is the relative permittivity of the material and is dimensionless. It should be observed that ϵ_r of free space is 1 and hence there is no polarization [13].

2.2.4 Complex Permittivity

If Eq.(2.16) is considered for periodic fields, the relationship in the frequency domain is given by

$$\mathbf{D} = \epsilon(\omega) \mathbf{E} \tag{2.17}$$

where ω is the angular frequency. The frequency dependent $\epsilon(\omega)$ is a complex property given by

$$\epsilon(\omega) = 1 + \int_0^\infty f(\tau) e^{j\omega\tau} d\tau \tag{2.18}$$

where τ is the relaxation time of the medium and $f(\tau)$ is a function of time and the properties of the medium. When periodic fields are considered, the permittivity is a function of the field frequency and material properties. The permittivity can then be described by a complex relationship

$$\epsilon(\omega) = \epsilon'(\omega) + j\epsilon''(\omega) \tag{2.19}$$

where j is the imaginary unit $\sqrt{-1}$ [14].

If a parallel-plate capacitor connected to an AC source is considered as in Figure 2.2, with an ideal dielectric material, the current would lag the voltage by 90^o. But if the dielectric material has a complex permittivity the current can be resolved into two components as seen in the phasor diagram in Figure 2.3. The current components are given as

$$I_1 = U\omega C_0 \epsilon' \tag{2.20}$$

$$I_2 = U\omega C_0 \epsilon'' \tag{2.21}$$

where U is the peak voltage applied across the dielectric in V and C_0 is the vacuum capacitance in F. The vacuum capacitance is the resulting capacitance if ϵ_r is set to 1 in Eq.2.2. The current component I_2 is in phase with the applied voltage and hence gives rise to losses. The current phasor will then be at an angle of $90 - \delta$, where δ is called the loss angle and is described by

$$\tan(\delta_0) = \frac{\epsilon''}{\epsilon'} \tag{2.22}$$

where $\tan(\delta_0)$ is sometimes referred to as the dissipation factor[15]. When considering power capacitors, the dissipation factor is usually given in $W/kvar$. The notation *var* stands for volt-ampere reactive and is a unit which reactive power is expressed in [11].

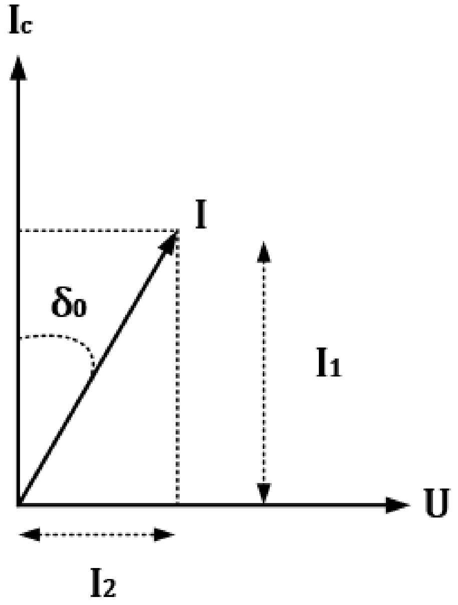

Figure 2.3: Phasor diagram of the current components for a parallel-plate capacitor connected to an AC voltage source. The angle δ is shown increased for clarifying purpose.

In dielectrics at low frequencies, it is difficult to separate the polarization and conduction mechanisms [16]. A frequency dependent complex conductivity related to both mechanisms can be stated as follows

$$\sigma(\omega) = j\epsilon_0\epsilon(\omega) \tag{2.23}$$

2.3 Metallized Polymer Film Capacitors

The capacitors integrated in the single valve cells seen in Figure 2.1, are in reality capacitor banks consisting of several capacitor units connected in series. Two photographs can be seen in Figure 2.4 of a capacitor bank (1) and a unit with the case open (2). The displayed bank is made up of 8 capacitor units and weighs over 1000 kg. One unit consists in turn of a large number of capacitor elements connected in parallel with a two-sided contact design. This contact design is a busbar-system of copper. The elements and the busbar-system are placed in an aluminum case and filled with Polyurethane resin (PUR) which is the yellow domains in (2). The PUR fills up the space inside the case and serves as mechanical support to keep the elements in place and prevents oxidation of the metallized polymer films.

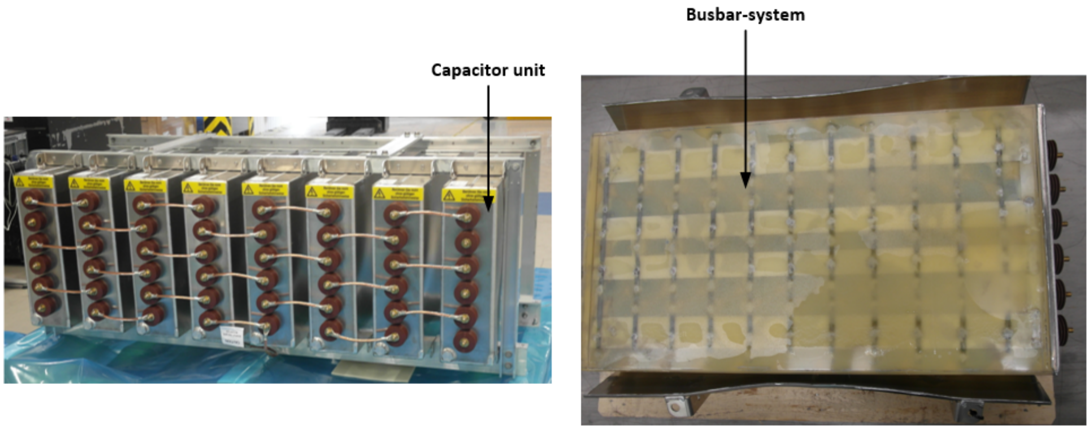

1) 2)

Figure 2.4: Photograph of a capacitor bank (1) and a capacitor unit with the aluminum case open (2).

In Figure 2.5 one capacitor element, one element without cover film, one plastic bobbin and one plastic bobbin with film wounded on it are shown. First one should look at (1) where one complete element are shown as it is utilized in the HVDC light application. The contacts at the top and bottom (not shown) are of zinc which is sprayed on to ensure a good electrical contact. Additionally the outermost layer is marked, which is a cover film to keep a high pressure inside the dielectric and to obtain electric insulation towards surrounding parts. Second one should look at (2), one element without the cover film. The partly unrolled shiny thin films is the dielectric of metallized polymer film. Thirdly one should look at (3) where the small plastic bobbin is shown and it can be noted that the thickness of the plastic bobbin is small in comparison to the element. At last one should look at (4) where just a few turns of films are wounded on the bobbin are shown. The dielectric consists of two metallized polymer films wounded in several turns (≈3000) on a bobbin.

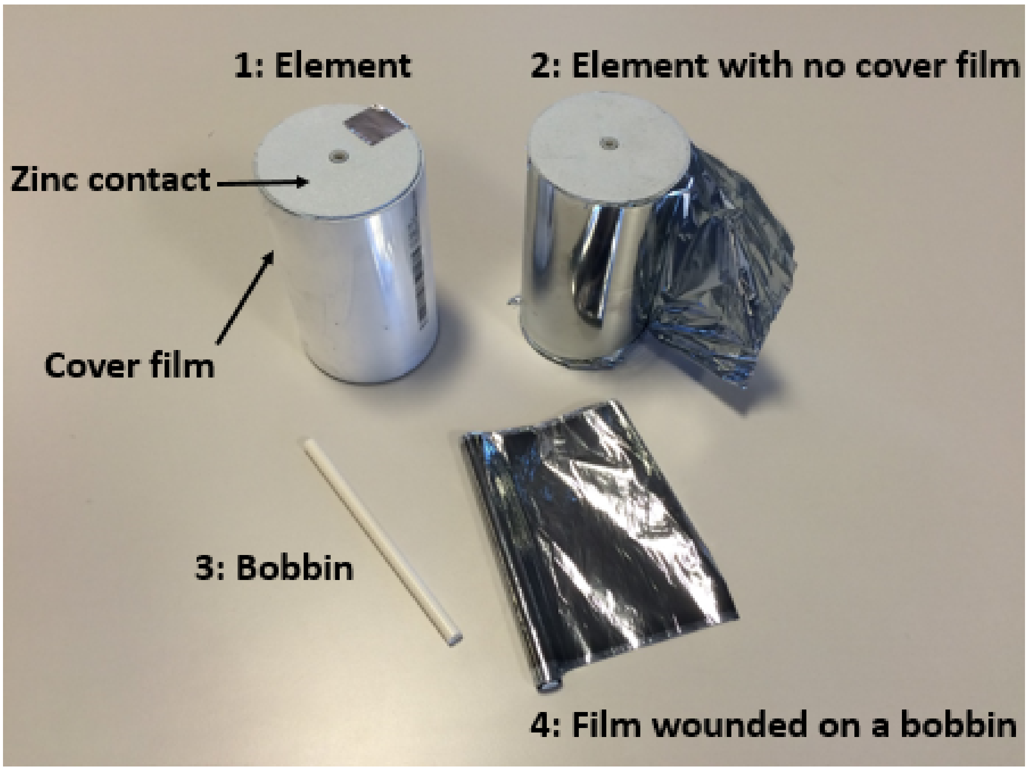

Figure 2.5: Photograph of a capacitor element (1), a capacitor element without cover film (2), a plastic bobbin (3) and part of the two films wounded on a plastic bobbin (4).

The polymer film is of Polypropylene (PP) which is characterized by low dielectric loss ($tan(\delta_0) = 2 \cdot 10^{-4}\ W/kvar$), a high electrical breakdown strength ($640V/\mu m$) and a relative permittivity of $\epsilon_r = 2.2$ [17]. The PP films are very thin and have a thickness of some μm. Thin layers (in the range of nm) of zinc-aluminum alloy($\approx$ 5 % Aluminum) are evaporated on the surface of the PP films. These thin layers acts as electrodes when the capacitor is operated. The metallization can either be unsegmented or segmented. If it is segmented then the metallization is evaporated onto the surface of the film in a pattern. The dielectric of the capacitor of interest consist of two metallized films placed on top of each other.

Thin metallized films are often described by their sheet resistance which is a measured quantity. It is the average resistivity over the sample thickness. The sheet resistance is given as

$$R_{sheet} = \frac{1}{\sigma m_{th}} \tag{2.24}$$

where R_{sheet} is the sheet resistivity in $\Omega/square$, σ is the conductivity in $Ssquare/m$ and m_{th} is the thickness of the metal layer in m. The square in the unit of sheet resistivity is an arbitrary square over a sample which the resistance is measured[18]. A top view of the two films can be seen in Figure 2.6 where the two films are placed on a light table to clearly visualize the metallization. Film A is segmented and the metallization has a grid like pattern of small squares. It has an heavy edge (increased thickness of the metallization) and a central margin with no metallization.

Film B is unsegmented and the metallization is uniform. The edges of Film B are called lateral margins and are not metallized but unfortunately this is not possible to see in the figure. The sheet resistance profile of Film A is low at the heavy edge and high between the heavy edge and central margin. Film B on the other hand has a constant resistance profile. A summary of the typically sheet resistances are given in Table 2.2.The active domain of Film A has a large resistance due to the segmentation. Two important aspects of the segmentation are the loss of capacitance (typically 3-5 %) and the increase in resistive loss by a gate factor (typically 2-3 times). These effects occurs because some of the metallized area is lost.

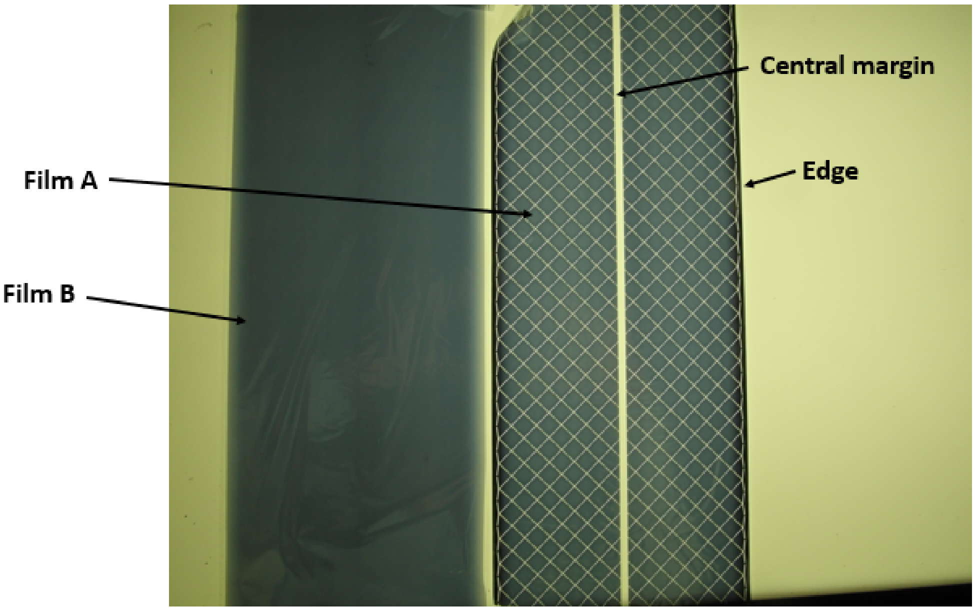

Figure 2.6: Photograph of Film A and Film B placed on a light table to visualize the difference between segmented and unsegmented metallization.

Table 2.2: Summary of the sheet resistances of different domains of the films.

Domain	**R**$_{sheet}$ $(\Omega/square)$
Film A - edge	2-4
Film A - active	27-45
Film B	9-15

The dielectric arrangement by placing the two films on top of each other and wound them on a bobbin, results in a parallel-plate capacitor of 500-600 m length if it would be rolled out. A cross section of the bobbin with one layer each film is illustrated in Figure 2.7. It is shown how the films are placed on the bobbin in layers and that Film A is wider than Film B. Furthermore, the central margin of Film A is shown (the electrodes are not continuously along the film). The electrode of Film B is not at contact to the applied potentials at the top and bottom and hence at floating potential. The electrodes of Film A is arranged to form two internal series connections by inserting a central margin which can be seen in Figure 2.8. This illustration is at the center of the films, to visualize the electric field. It can be seen at the right, that the field will be perpendicular to the electrodes and points away from the positive electrode towards the floating electrode. At the left, the field points towards the grounded electrodes. As a result two internal series connected capacitors are formed and the equivalent electrical circuit is seen in (2). One advantage of using internal series is that the voltage across the films and the electric field strength are reduced. The capacitance of a wounded parallel-plate capacitance can be computed from geometrical and material properties [19]. The capacitance of one internal series is given as

$$C_{s1} = 2 \cdot \frac{\epsilon_0 \epsilon_r W l}{d} \tag{2.25}$$

where W is the effective width of one series in m (width over which metalized electrodes face each other at upper or lower part), d is the film thickness in m and l is the length of one film. The factor 2 comes from the fact that there is a contribution from each layer to both above and below. The total capacitance can be calculated by dividing Eq. 2.25 with 2 (series connection of two capacitors) as follows

$$C_{analytical} = \frac{C_{s1}}{2} \tag{2.26}$$

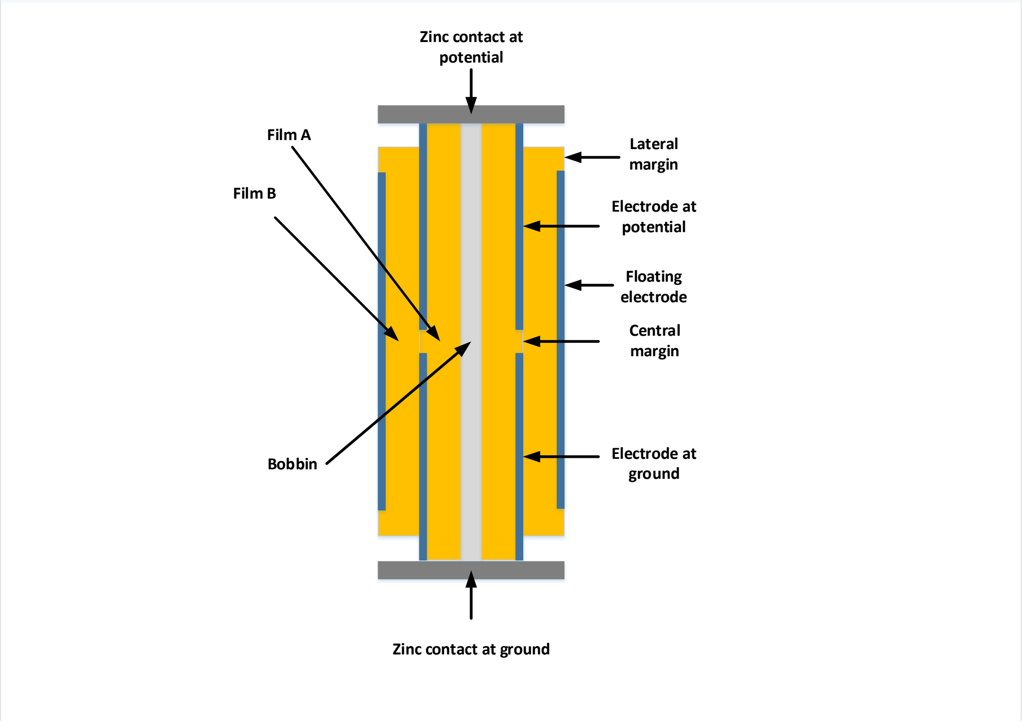

Figure 2.7: Illustration of the cross section of one element, showing the zinc contacts and the bobbin with one layer of Film A and Film B. Yellow is PP and blue is metallization.

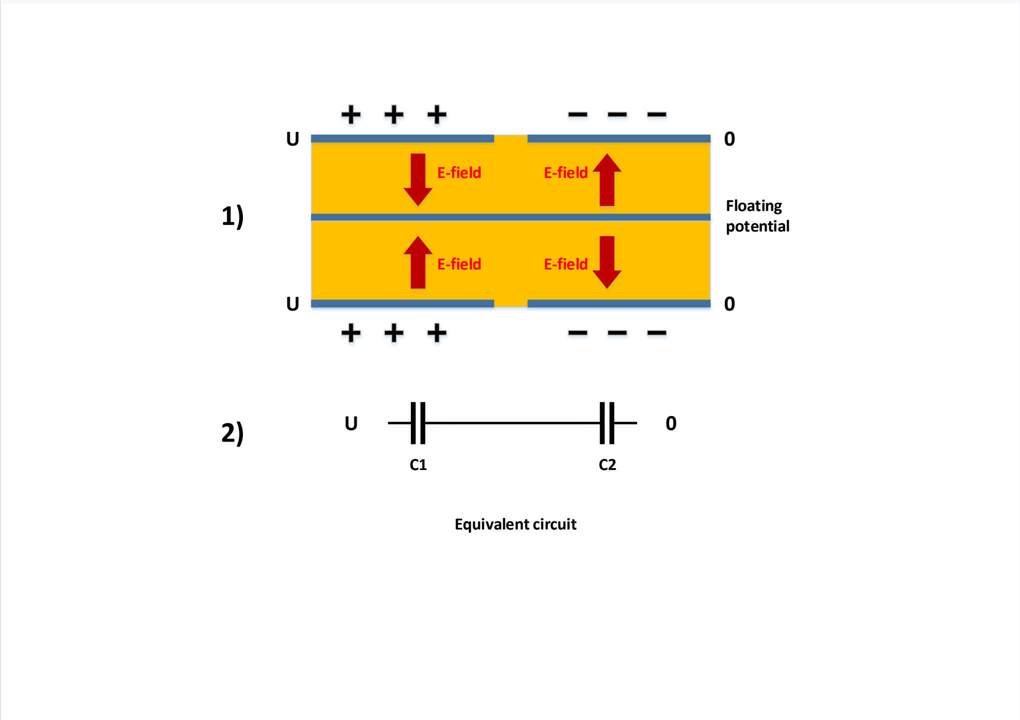

Figure 2.8: Illustration of 1) a capacitor with one internal series connection and the direction of the electric field (red arrows) and 2) the equivalent circuit of the arrangement. Yellow is PP and blue is metallization. U is a positive potential and 0 is ground.

2.3.1 Self-healing

Metallized film capacitors have the capacity to undergo a process called self-healing or clearing when voltage is applied. This process serves as a safety mechanism. As previously described the electrodes are evaporated zinc-aluminum alloy which are important for the self-healing process. If a localized breakdown occurs in the dielectric caused for example by particles or dielectric degradation, it results in a discharge of a portion of the stored charge. This give rise to a local increase in temperature and pressure, causing a puncture in the PP film and the metallization evaporates fast. Segmented film is divided into small segments, each segment having small current gates where the current needs to pass during charging or discharging. The current gates can be seen in Figure 2.9 before self-healing has occurred(1) and after self-healing (2). When a breakdown occurs in a segment, a clearing channel emerges and the current gates evaporates due to the much smaller cross section compared to a segment. When the current gates are disconnected, the failed local segment is insulated and no longer contribute to the capacitance. During operation self-healing will occur continuously and a small fraction of the capacitance are lost for each event [20]. This ability allows metallized film capacitors to be operated without external fuses, since breakdown can occur without the risk of short circuit in the dielectric.

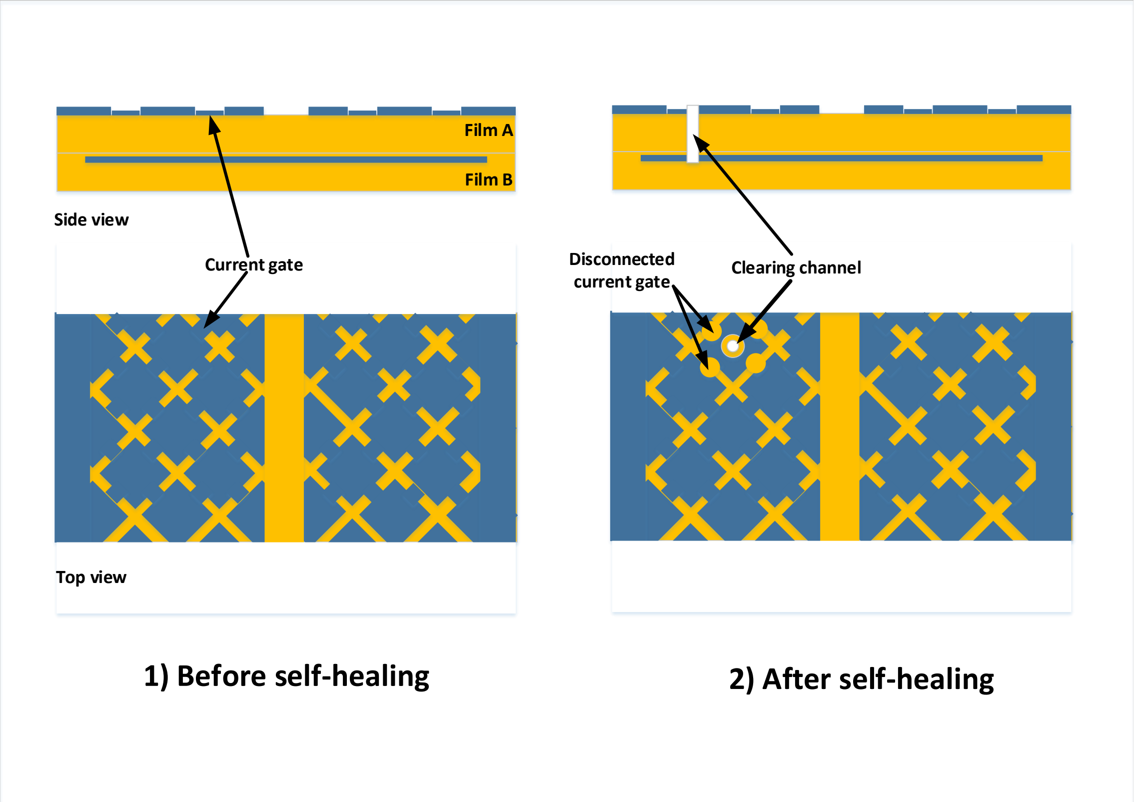

Figure 2.9: Schematic picture of self-healing for segmented film. Before self-healing has occurred (1) and after self-healing has taken place (2). Yellow is PP and blue is metallization.

2.3.2 Losses and Heating

During operation there will be losses occurring in the metallized film because of dielectric losses in the PP film and resistive losses in the metal layers when currents are flowing [21]. The total loss is given as

$$P_[tot = P_{res} + P_{diel} \tag{2.27}$$

where P_{tot} is the total loss in W. The average resistive loss when $\mathbf{J}(t)$ and $\mathbf{E}(t)$ are sinusoidal quantities is given by

$$P_{res} = \frac{1}{T}\int_0^T (\int_V \mathbf{J}(t) \cdot \mathbf{E}(t) dV)dt = Re(J(\omega) \cdot E(\omega)^*) \tag{2.28}$$

where P_{res} is the resistive loss component in W, Re is the real-part, $J(\omega)$ is the complex-frequency dependent current density in A/m^2, $E(\omega)$ is the complex-frequency dependent electric field in V/m and $*$ indicates the conjugate[22]. The dielectric loss described by the dissipation factor in Eq. 2.22 is given by

$$P_{diel} = tan(\delta_0)Q \tag{2.29}$$

where P_{diel} is the dielectric loss component in W and Q is the reactive power in var [21]. The reactive power in a capacitor is given by

$$Q = \omega C U_{rms}^2 \tag{2.30}$$

where U_{rms} is the root mean square voltage in V [11]. The total dissipation factor can then be stated as

$$tan(\delta) = \frac{P_{tot}}{Q} \tag{2.31}$$

where $tan(\delta)$ is the total dissipation factor in $W/kvar$, taken into account both the dielectric and resistive losses.

The losses result in generation of heat and the thermal conductivity is then an important factor when considering the temperature rise inside the dielectric. PP is an isotropic material and has the same thermal conductivity in all directions. But when PP is metallized, the thermal conductivity becomes anisotropic and is not the same in all directions and this will influence the thermal behaviour [23].

2.3.3 Lifetime

The hot spot temperature and temperature rise inside the dielectric are important to know when designing a capacitor. A lifetime estimation is provided by all manufactures of capacitors and these estimations are based on so called scaling laws. By testing a capacitor at a higher voltage than the rated, during a number of hours a scaling law can be derived from the results. These laws estimates when the capacitor has lost 5% of the rated capacitance. The scaling law that ABB uses is given as

$$L_5 = L_0 \left[\frac{E}{E_0}\right]^{-n} \cdot exp\left(\frac{-T}{A}\right) \tag{2.32}$$

where L_0 is a time constant,E is the electric field at rated operation ($E_0 = 200V/\mu m$), n is a fitting constant, T is the temperature in the dielectric at rated operation in $°C$ and A is a temperature constant. It can be seen that the temperature is a critical factor for the lifetime of the capacitor.

3

Modelling Procedures

In this chapter the multiscale approach is introduced and different COMSOL models are presented with implemented geometry, boundary conditions, material properties, mesh and study options.

3.1 Multiscale Computation Approach

For electrical and thermal simulations of a capacitor, the properties of interest are the electrical conductivity and the relative permittivity as well as the thermal conductivity. As described in section 2.3, the dielectric consists of a mix of two different materials, PP and zinc-aluminum alloy. This is a combination of a poorly conductive material (PP) and an highly conductive material (zinc-aluminum alloy) both in electrical and thermal terms. Additionally a capacitor element consists of different parts with large difference in dimensions. The radius of a capacitor element is in mm, the thickness of the PP film is in μm and the thickness of the metallic layers are in nm. Furthermore the dielectric consists of about 3200 turns wounded on a bobbin. It becomes evident that an element is difficult to model in a detailed approach. A possible approach is to use a computer software which solves PDEs by numerical methods. The finite element method allows modelling of dielectric mixtures to compute electric fields and current densities. Mixture of different dielectrics, mainly composite materials have been studied with the use of FEM based programs. Since FEM is a numerical method which divides a large domain into a number of small domains by meshing, it is evident that a detailed modelling of the PP film dielectric would require large computer power. One possible solution is to use a multiscale computation approach to overcome the described issues. This method has previously been used together with FEM based computational programs. A representative volume of a complex material can be implemented and computations can be performed to obtain effective properties[24] [25].

From studies on different scales, effective electrical and thermal properties as well as dielectric losses can be computed on a small scale, i.e some layers of the metallized films. The effective properties can be applied to a middle scale model (capacitor element) to compute losses. Finally the effective properties and losses can be implemented to a large scale model of a capacitor unit. The procedure can be seen in Figure 3.1 where the different scales are shown as well as dimensions of the geometries and the properties obtained at the different scales. It is important in the small scale model that given boundary conditions also are present in the large scale model.

This is to make sure that the electric field and potential distribution maintains their natural behaviour and are defined by material properties. This also applies for the thermal simulations, where it is desirable that the heat flux and temperature distribution maintains their natural behaviour. It is then possible to compute the effective properties and apply them to the middle and large scale models. The middle scale is not studied explicitly but is integrated in the large scale. Further, losses and capacitance are computed for the purpose of validation.

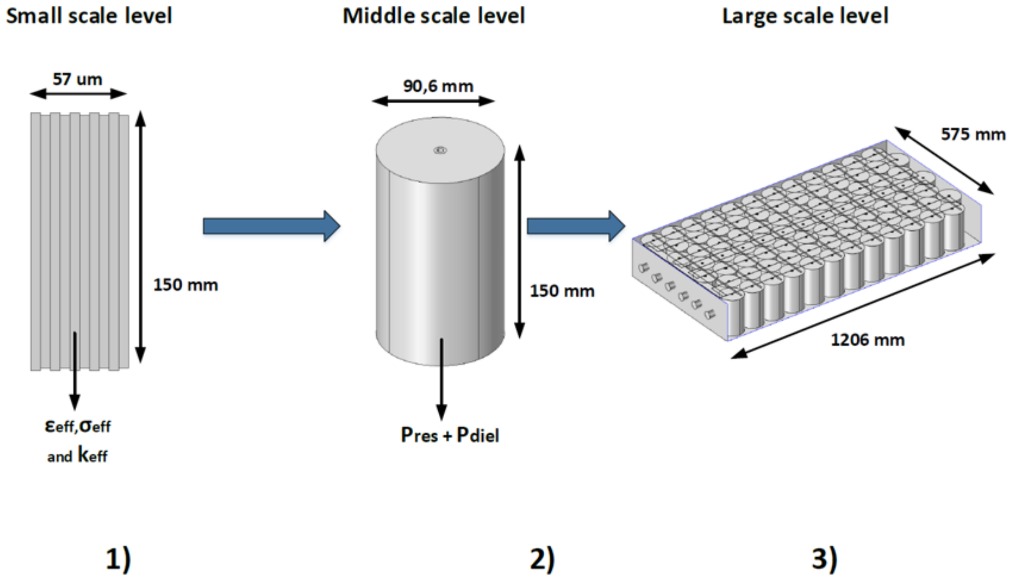

Figure 3.1: The different scale levels of a capacitor for multiscale modelling, metallized film dielectric (1), capacitor element (2) and capacitor unit (3).

3.1.1 Effective Properties

The effective electrical properties account for a mixture of materials and are describing the electrical behaviour. The properties can be obtained by different approaches once the potential distribution is computed [24]. In Figure 3.2 illustrations of the computation approaches are shown. The setup for computing electrical properties (ϵ and σ) is illustrated in (1). It can be seen that a current density flows in the z-direction, if a potential difference of 1 V is applied between the horizontal boundaries and a boundary conditions for electric insulation on the vertical boundaries. The resulting current density and electric field will be dependent on the properties of the materials in the geometry.

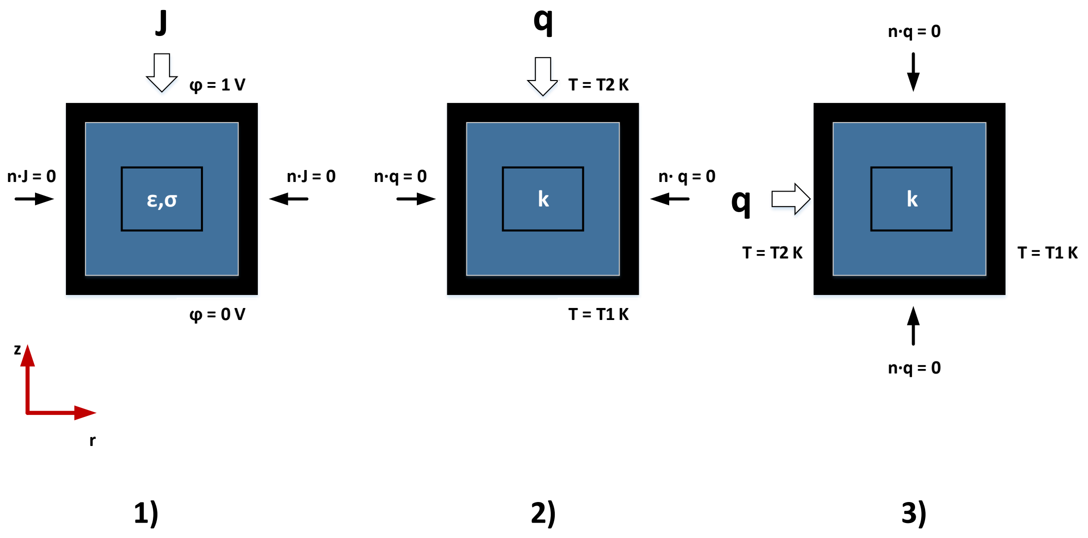

Figure 3.2: Illustration of the computation approaches and boundary conditions. Setup for computation of electrical properties (1) and thermal properties in z-direction (2) and r-direction (3).

If the potential applied is sinusoidal, the effective properties will be frequency dependent. It is possible to compute effective electrical properties by first computing the average current density and the average electric field in the direction of interest

$$J(\omega) = \frac{I(\omega)}{A_{cs}} \tag{3.1}$$

$$E_{avg} = \frac{1}{vol}\int E_z dv \tag{3.2}$$

where $I(\omega)$ is the current in A, A_{cs} is the cross section area of the horizontal boundary in m^2, E_z is the z-component of the electric field in V/m and vol is the volume of the geometry in m^3. From the average parameters the effective conductivity and the effective permittivity can be obtained by inserting the average values into Eq.(2.8) and Eq.(2.23) as

$$\sigma_{eff}(\omega) = \frac{J(\omega)}{E_{avg}} \tag{3.3}$$

$$\epsilon_{eff}(\omega) = \frac{\sigma_{eff}}{j\omega\epsilon_0} \tag{3.4}$$

A similar approach can be used to compute the effective thermal property which can be obtained once the temperature distribution is known. Thermal conductivity of the metallized PP films are of interest when studying the temperature distribution inside the dielectric. In this case the z and r components are of interest. If a temperature difference of 1 K $(T_1 - T_2)$ is applied between the horizontal boundaries and a boundary condition for thermal insulation is set on the vertical boundaries, a heat flux will flow in the z-direction which is illustrated in Figure 3.2 (2). If the temperature difference is instead applied between the vertical boundaries and thermal insulation is set on the horizontal boundaries, a heat flux will flow in the r-direction as illustrated in Figure 3.2 (3). The heat flux is dependent on the material properties in the geometry and is given by Fourier's law as

$$\mathbf{q} = -k\nabla T \tag{3.5}$$

where $\mathbf{q}$ is the heat flux vector in W/m^2, k is the thermal conductivity in W/mK ∇T is the temperature gradient in K/m. The effective thermal conductivity can be obtained by first computing the average heat flux flowing across a surface and the temperature gradient in the direction of interest as follows

$$q_{avg} = \frac{1}{A_{cs}} \int \mathbf{q}_{comp} ds \tag{3.6}$$

$$\nabla T = \frac{T_1 - T_2}{L} \tag{3.7}$$

where q_{avg} is the average heat flux in W/m^2, $\mathbf{q}_{comp}$ is the heat flux component in the direction of interest and L is the distance in m, between the boundaries where T_1 and T_2 are applied. Once the average heat flux and temperature gradient are computed, the effective thermal conductivity's can be computed by rearranging Eq.3.5 [26]. The effective thermal conductivity in the z and r-direction are computed as follows

$$k_z = \frac{q_z \cdot L_z}{T_1 - T_2} \tag{3.8}$$

$$k_r = \frac{q_r \cdot L_r}{T_1 - T_2} \tag{3.9}$$

where q_r and q_z are the average heat fluxes in r and z-directions in W/m^2.

3.2 Computer Implementation

The software COMSOL multiphysics can be used to study a wide range of scientific and engineering phenomena. The foundations of the program are partial differential equations (PDEs) which are assembled and solved by a set of numerical analysis tools. The program utilizes so called physics interfaces which are nodes and settings containing sets of equations and variables for specific areas of physics. To study a model of interest, a geometry needs to be built in the desired space dimensions and thereafter material properties of importance to the physics of interest needs to be provided. Next a physics interface needs to be selected and boundary conditions applied. The two fundamental boundaries are exterior boundaries and interior boundaries. An exterior boundary is an outer boundary of the modeling domain and an interior boundary is an interface which divides two domains in the geometry.

On the selection where a physics interface is active, the interior behaviour is decided by the equations of the interface and the material properties. The program enables two main implementations of conditions for exterior boundaries, flux conditions and constraints.

- Flux conditions are used to describe the interaction of the model and the surroundings at the boundary, often applied flux or current. This type of boundary condition is often referred to as Neumann boundary condition.
- Constraints implement the expected values of the dependent variables on the boundary to describe the result of the interaction between the model and its surrounding. This type of boundary condition is often referred to as Dirichlet boundary condition.

Once the boundary conditions are selected, a meshing sequence is applied. This enables discretization of the geometry into small units. A solver should also be provided and then COMSOL can solve the model by using the finite element method [27].

3.2.1 The Electric Currents Interface

The electric currents interface computes electric fields, currents and potential distributions in conducting media. It also enables computation of power dissipation rising from Joule heating. Models can be studied as stationary as well as in frequency and time-domain. The depended variable is the electric potential and the interface solves an equation based on Ohm's law and the displacement current. The main node of the interface adds the following set of equations in the frequency domain

$$\nabla \cdot \mathbf{J} = Q_j \tag{3.10}$$

$$\mathbf{J} = (\sigma + j\omega\epsilon_0\epsilon_r)\mathbf{E} + \mathbf{J}_e \tag{3.11}$$

$$\mathbf{E} = -\nabla\varphi \tag{3.12}$$

where Q_j is a distributed current source in A/m^3 (it is 0 at default if not specified by a boundary condition), $j\omega\epsilon_0\epsilon_r\mathbf{E}$ is the displacement current in A/m^2 and $\mathbf{J}_e$ is an externally generated current density (it is also specified by a boundary condition, otherwise 0) [22]. Eq 3.10 is the same as Eq 2.9 if there exist no distributed current sources in the model and hence $Q_j = 0$. The second equation is of great importance, because this is how the current density is defined in the interface. It says that the current density in the system to be studied is a summation of 3 sources. The first term ($\sigma\mathbf{E}$) is the current density due to free charges described by Eq 2.8, the second term ($j\omega\epsilon_0\epsilon_r\mathbf{E}$) is the displacement current which adds the contribution of the time varying electric displacement field and the third term only exists if there is an externally generated current density implemented in the model. The last equation 3.12, is the same as Eq 2.10 and describes how the electric field is computed in the interface.

Numerical solutions of the electric potential is based on solving an equation resulting of combining Eq 3.10, Eq 3.11 and Eq 3.12 (if $Q_j = 0$ and $\mathbf{J}_e$ is not implemented). The combination results in

$$\nabla \cdot (\sigma \nabla \varphi + j\omega\epsilon_0\epsilon_r \nabla \varphi) = 0 \tag{3.13}$$

where it can be seen that the potential is dependent on the material properties. This equation is solved by COMSOL and when the potential distribution is known, other properties of interest can be computed [24].

3.2.2 Boundary Conditions - Electric Currents

Boundary conditions are applied as nodes in COMSOL and the following are of interest when modelling electric currents and electric fields,

Terminal
This boundary node can be used to specify a voltage or current on a boundary or a domain. A current can be specified to flow from the terminal on a boundary. Additionally it enables the computation of lumped parameters of a system as for example the impedance.

Electric Shielding
This boundary node is used to model a highly conductive thin layer and reduces the number of mesh elements by approximating a thin layer. The thickness of the layer, conductivity and relative permittivity are provided to the node. The following equation is implemented at the boundary

$$\mathbf{n} \cdot (\mathbf{J}_1 - \mathbf{J}_2) = -\nabla_t d(\sigma_s + j\omega\epsilon_{0rs})\nabla_t \varphi \tag{3.14}$$

where $\mathbf{n}$ is the normal vector, ∇_t is the tangential gradient, d is the thickness of the layer, σ_s is the conductivity of the layer, ϵ_{rs} is the relative permittivity of the layer.

Electric Insulation
This boundary node adds the following equation to a boundary

$$\mathbf{n} \cdot \mathbf{J} = 0 \tag{3.15}$$

When this node is active, no electric currents flows into the boundary [22].

3.2.3 The Heat Transfer in Solids Interface

The heat transfer in solids interface can be used to model heat transfer by conduction, convection and radiation. The dependent variable is the temperature and the interface solves an equation based on the heat equation. The main node is named solid and adds the following two equations

$$\rho C_p \frac{\partial T}{\partial t} + \rho C_p \mathbf{u} \cdot \nabla T + \nabla \cdot \mathbf{q} = Q \tag{3.16}$$

$$\mathbf{q} = -k \nabla T \tag{3.17}$$

where ρ is the solid density in kg/m^3, C_p is the heat capacity at constant pressure in J/mK, T is the temperature in K, $\mathbf{u}$ is the velocity field arising when parts of the model are moving in m/s, Q is a heat source (or sink) in W/m^3, $\mathbf{q}$ is the heat flux in W/m^2 and k is the thermal conductivity in W/mK (scalar or tensor)[28]. For a steady state problem, the temperature will not change with time and the first term disappears in Eq.3.16. Furthermore, if there are no parts of the model moving the second term also disappears. By inserting Eq.3.17 into Eq. 3.16 the following is obtained

$$-k\nabla^2 T = Q \tag{3.18}$$

this equation is solved by COMSOL and when the temperature distribution is known other properties of interest can be obtained. The temperature distribution in stationary is governed by the k of materials in the model and the boundary conditions.

3.2.4 Boundary Conditions - Heat Transfer in Solids

The following boundary nodes are of interest when modelling heat transfer,

Heat Flux

This boundary node is used to add heat flux across a boundary. The node provides a setting to insert convective heat flux across a boundary by specifying the heat transfer coefficient and the external temperature. The following equation is specified at a boundary when this node is active

$$-\mathbf{n}\cdot\mathbf{q} = h\cdot(T_{ext} - T) \tag{3.19}$$

where h is the heat transfer coefficient in W/m^2K and T_{ext} is the external temperature in K.

Heat Source

This boundary node is used to add heat generation within a domain. The setting, heat rate enables the implementation of generated heat within a specified domain as

$$Q_0 = P_0/V \tag{3.20}$$

where Q_0 is the heat rate of the selected domain in W/m^3, P_0 is the power in W and V is the volume of the selected domain. The heat source adds to the right hand side of Eq.3.16.

Thin Layer

This boundary node can be used to model a thin layer of a material on an internal or external boundary to reduce the number of mesh elements. The thickness of the layer and the thermal conductivity of the material are implemented. Only tangential heat flux is considered(indicated by tangential gradient ∇_t) and temperature difference and heat flux across the boundary are not considered. The following equations are implemented at the boundary

$$-\mathbf{n}\cdot\mathbf{q} = d_s Q_s - \nabla_t\cdot\mathbf{q}_s \tag{3.21}$$

$$\mathbf{q}_s = d_s k_s \nabla_t T \tag{3.22}$$

where d_s is the thickness of the layer in m, ∇_t is the tangential gradient and k_s is the thermal conductivity of the thin layer in W/mK.

Thermal Insulation
This boundary node adds the following equation to a boundary

$$-\mathbf{n} \cdot \mathbf{q} = 0 \tag{3.23}$$

when this node is used, no heat flux flows into the boundary [28].

3.2.5 Multiphysics Coupling

Two multiphysics nodes used to couple electric losses to the heat transfer interface are

Electromagnetic Heat Source
It is possible to couple electric currents and heat transfer in solids by adding a multiphysics node. This multiphysics coupling node adds the contribution of Joule heating when the heat transfer in solids is computed. If only heating due to resistive losses are considered the node adds an heat source to Eq. 3.16 as

$$Q_{rh} = \frac{1}{2} Re(J \cdot E^*) \tag{3.24}$$

where Q_{rh} is the heat source due to resistive losses in W/m^3, * is the conjugate and Re is the real part.

Boundary Electromagnetic Heat Source
This boundary node adds the electrical losses on a boundary as

$$-\mathbf{n} \cdot (-k \nabla T) = Q_b \tag{3.25}$$

where Q_b is a heat source on the boundary where the node is active in W/m^2 [28].

3.3 Small Scale - Electrical Model

The capacitor elements of interest are cylindrical and therefore a geometry of the dielectric is created in the space dimension, 2D axisymmetric. The geometry of the dielectric described in section (2.3), in the space dimension 2D axisymmetric can be seen in Figure 3.3. Five layers each of Film A and B are chosen as a representative volume of the dielectric. The figure is a cross section of the cylindrical shaped geometry. The outer radius of one capacitor element is approximately 43 mm and here the layers are placed in the middle at 20 mm. The r-axis is increased 1000 times to clearly show the geometry. The first layer is Film A and it can be seen that the rectangle is wider than the second one which is Film B. The width (z-direction), the thickness (r-direction) and other dimensions of the films are presented in Table

3.1. Different points are placed on the boundaries for each film and the points will be used to implement the metallization. The heavy edges of Film A is referring to a lower resistance and the active width is referring to segmention. The central margin is the lengt at the center where no metallization is implemented. Film B has a shorter width and only two points. Metallization is implemented between the points and hence no metallization at the edges (laterl margin). The total length of one film in the table is referring to the length if the layers are rolled out. This comes from the fact that the geometry is in cylindrical coordinates and only a cross section is shown in the figure.

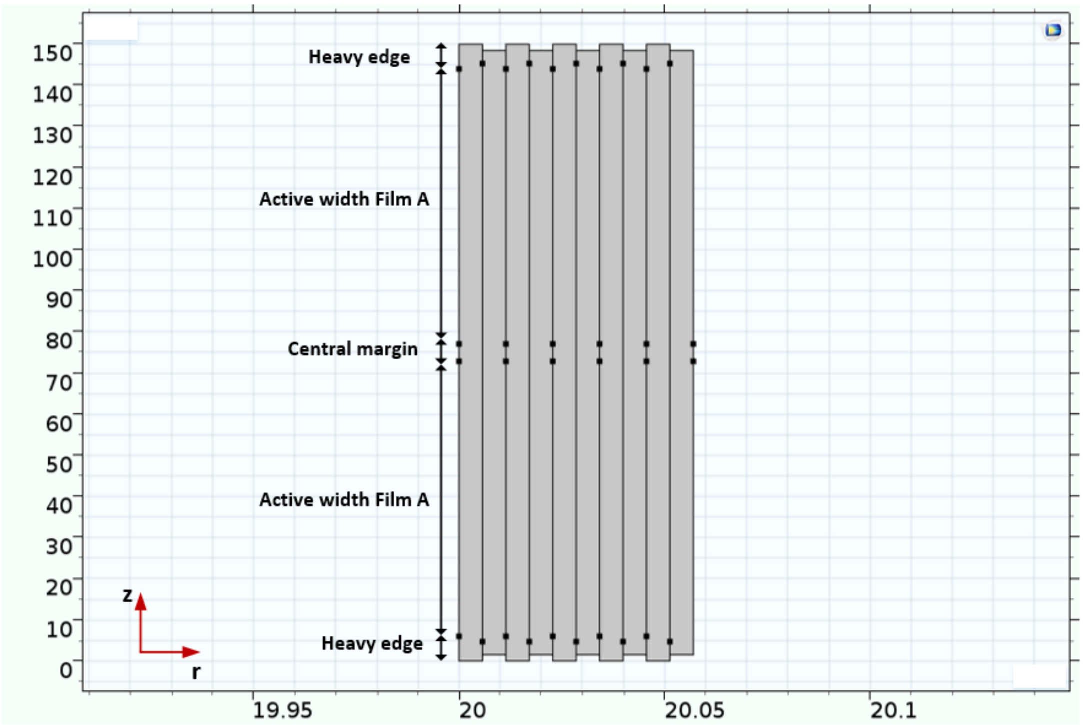

Figure 3.3: Illustration of the geometry of the dielectric for electrical simulations. The scale of the z and r-axis are 1,1000 in *mm*.

Table 3.1: Summary of different dimensions of the geometry.

Description	**Dimension**
Width of Film A	150 mm
Width of Film B	147 mm
Width of heavy edge	6 mm
Width of active width Film A	67,4 mm
Length of central margin	4,2 mm
Length of lateral margin	3,2 mm
Film thickness	5,7 μm
Total length of one film	0,63 m

3.3.1 Meshing of the Small Scale Electrical Model

The mesh applied to the geometry seen in Figure 3.3 is a structured quadrilateral mesh, which looks like small squares. The mesh can be seen in Figure 3.4, the entire geometry (1) and a zoom in at one of the corners (2). It can be seen from both the Figures that the vertical mesh segments are made of straight lines and the horizontal has a slightly crisscross pattern. The quality of the mesh is a bit low but this particular geometry is hard to mesh proper since the large difference in scale (*mm* versus *µm*). Furthermore, the difference in width of the films increase the difficulty. Since the computed properties (losses and capacitance) matches well, the mesh quality seems not to influence the results. A summary of parameters and statistics of the mesh can be seen in Table 3.2.

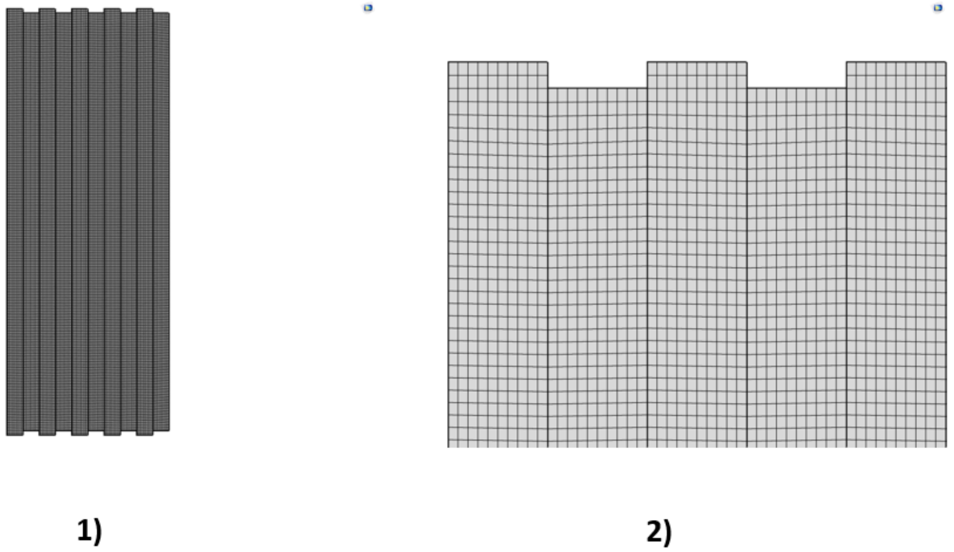

Figure 3.4: The mesh of the small scale electrical model, complete mesh (1) and zoom in (2).

Table 3.2: Summary of parameters and statistics of the mesh of the small scale electrical model.

Element size parameters	
Max element size	1,05 *mm*
Min element size	0,0005 *mm*
Max element growth rate	1,05
Curvature factor	0,15
Complete mesh statistics	
Number of elements	20800
Min element quality	0.01055
Avg element quality	0.1476
Element area ratio	0,8784

3.3.2 Physical Interface and Boundary Conditions

To study the electric field and the current density the interface electric currents described in section 3.2.1 is applied to the model. The important material properties for this interface are electrical conductivity σ and relative permittivity ϵ_r. In Figure 3.5 an illustration of the study domain and the boundary conditions are seen. It can be noted that potential is only applied to the horizontal exterior boundaries of Film A since only Film A is in contact with the zinc-contacts of an element. The blue metal layers are implemented with a boundary conditions and have zero thickness to reduce the number of mesh elements. This is applicable since the difference in thickness between the PP films and the metal layers is a factor of $10^{3]}$. The blue metal layers of Film A has two different parts where the edge is thicker. This is implemented with a lower sheet resistance. Electric potential and ground are applied to the vertical exterior boundary of Film B (black lines) to maintain the natural behaviour of the electric field. It should be highlighted that no current is flowing in these domains. Additionally electric insulation is applied to the horizontal exterior boundaries of Film B (top and bottom). The polymer film has the electrical properties $\sigma_{PP} = 3 \cdot 10^{-15} S/m$ and $\epsilon_{PP} = 2,2$. The electric conductivity of the metal is $\sigma_{sheet} = 1/\rho_{sheet}$, where ρ_{sheet} is calculated from Eq.2.24. It should be highlighted that the sheet resistance of Film A is multiplied by a gate factor (G_{factor}) to account for segmentation. The interface is solved in frequency domain and the boundary and initial conditions are implemented as follows

1. Boundary Conditions
    - **Terminal**: $\varphi_1 = 1\ sin(2\pi f)\ V$ applied to the top horizontal exterior boundaries of Film A.
    - **Electric potential**: $\varphi_2 = 1\ sin(2\pi f)\ V$ applied to the vertical exterior boundary of Film B.
    - **Ground**: $\varphi_3 = 0\ V$, applied to the bottom horizontal exterior boundaries of Film A.
    - **Electric shielding edge**: to the edge metal boundaries of Film A, d_s= 20 nm, $\epsilon_{rs} = 1$ and $R_{sheet} = 3\ \Omega$
    - **Electric shielding Film A**: to the active metal boundaries of Film A, d_s= 20 nm, $\epsilon_{rs} = 1$, $R_{sheet} = 9 - 15\ \Omega$ and $G_{factor} = 2,8 - 3,2$
    - **Electric shielding Film B**: to the metal boundaries of Film B, d_s= 20 nm, $\epsilon_{rs} = 1$ and $R_{sheet} = 9 - 15\ \Omega$
    - **Electric insulation**: to remaining exterior boundaries.
2. Initial Conditions
    - **Initial values**: 0 V applied to all domains.

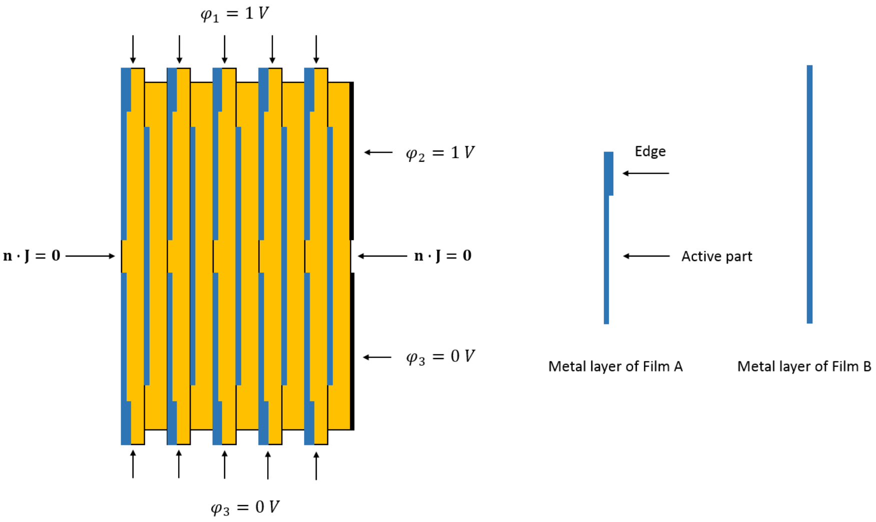

Figure 3.5: Illustration of the boundary conditions for the electrical simulations where the parts of the metal layers are highlighted. Yellow is PP, blue is metal and black is a boundary of constant potential where no current is flowing.

3.4 Small Scale - Thermal Model

The geometry for the thermal simulations can be seen in Figure 3.6. As for the electrical model, the geometry is in 2D axisymmetric space dimensions.

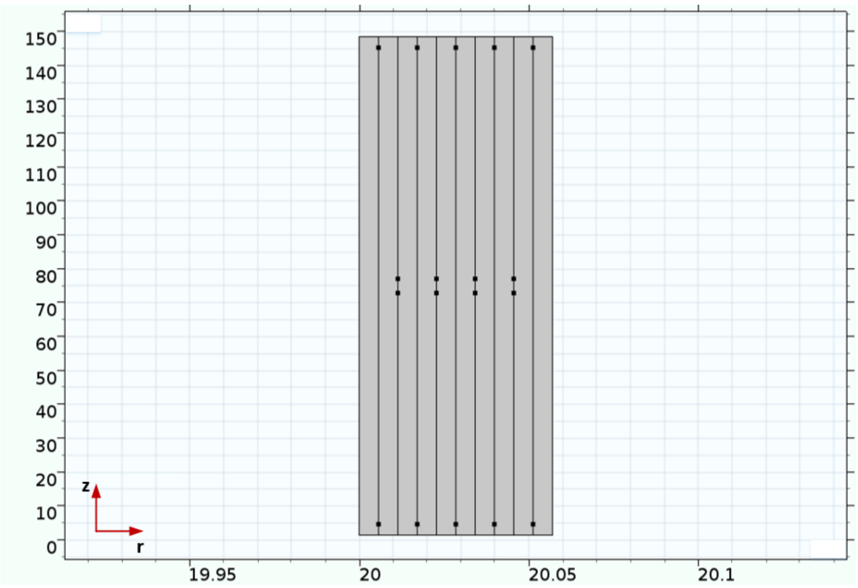

Figure 3.6: Illustration of the geometry of the dielectric for thermal simulations. The scale of the z and r-axis are 1,1000 in *mm*.

3.4.1 Meshing of the Small Scale Thermal Model

A similar meshing approach is used for the thermal model as for the electrical model. The complete mesh can be seen in Figure 3.7. The geometry is a slightly smaller then geometry for the electrical simulations and less mesh elements are needed. The average quality is a bit lower compared to the mesh for the electrical simulations. A summary of the parameters and statistics of the mesh is presented in Table 3.5.

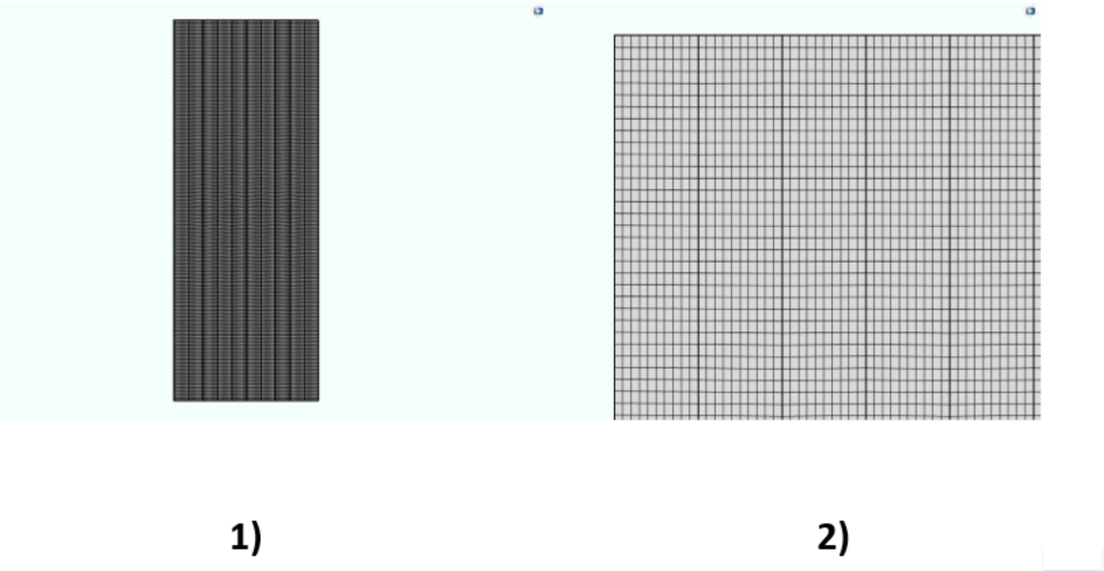

Figure 3.7: The mesh of the small scale thermal model, complete mesh (1) and zoom in (2).

Table 3.3: Summary of parameters and statistics of the mesh of the small scale thermal model.

Element size parameters	
Max element size	0,8 *mm*
Min element size	0,0005 *mm*
Max element growth rate	1,05
Curvature factor	0,15
Complete mesh statistics	
Number of elements	18600
Min element quality	0,01345
Avg element quality	0,1223
Element area ratio	0,8811

3.4.2 Physical Interface and Boundary Conditions

To study the temperature distribution and heat flux, Heat transfer in Solids described in section 3.2.3 is applied to the geometry. A temperature difference is applied between the horizontal exterior boundaries of the geometry to compute the thermal conductivity in the z-direction. For computation of the thermal conductivity in the r-direction, a temperature difference is instead applied between the vertical exterior boundaries. An illustration of the boundary conditions can be seen in Figure 3.8, in the z-direction (1) and in the r-direction (2). The blue marked boundaries are the metallic layers. As for the electrical model, the metallic layers are implemented by a similar boundary condition to reduce mesh elements. The relevant material property of the PP films is thermal conductivity, k_{pp} = 0,17-0,22 W/mK.The zinc-aluminum alloy consist of 5 % aluminum and the resulting thermal conductivity is calculated as

$$k_{metal} = k_{zn} + 0,05k_{Al} \tag{3.26}$$

where k_{metal} = 131,9 W/mK and the following values are used k_{zn}=120 W/mK and k_{Al}=238 W/mK. The interface is solved in stationary and the boundary and initial conditions implemented to compute the effective thermal conductivity in the z-direction are as follows

1. Boundary Conditions
    - **Temperature**: $T_1 = 21\ °C$ applied to the top horizontal exterior boundaries.
    - **Temperature 2**: $T_2 = 20\ °C$ applied to the bottom horizontal exterior boundaries.
    - **Thermal isolation**: To the vertical exterior boundaries.
    - **Thin layers**: Thermally thin approximation to the interior metal layers, $d_s = 20\ nm$ and k = 131,9 W/mK.

2. Initial Conditions
    - **Initial values**: 20 $°C$ applied to all domains.

The boundary and initial conditions implemented to compute the effective thermal conductivity in the r-direction are as follows

1. Boundary Conditions
    - **Temperature 1**: $T_1 = 21\ °C$ applied to the first exterior vertical boundaries.
    - **Temperature 2**: $T_2 = 20\ °C$ applied to the second exterior vertical.
    - **Thermal isolation**: To the exterior top and bottom horizontal boundaries.
    - **Thin layers**: Thermally thin approximation to the metal layers, d_s = 20 nm and k = 131,9 W/mK

2. Initial Conditions
    - **Initial values**: 20 $°C$ applied to all domains.

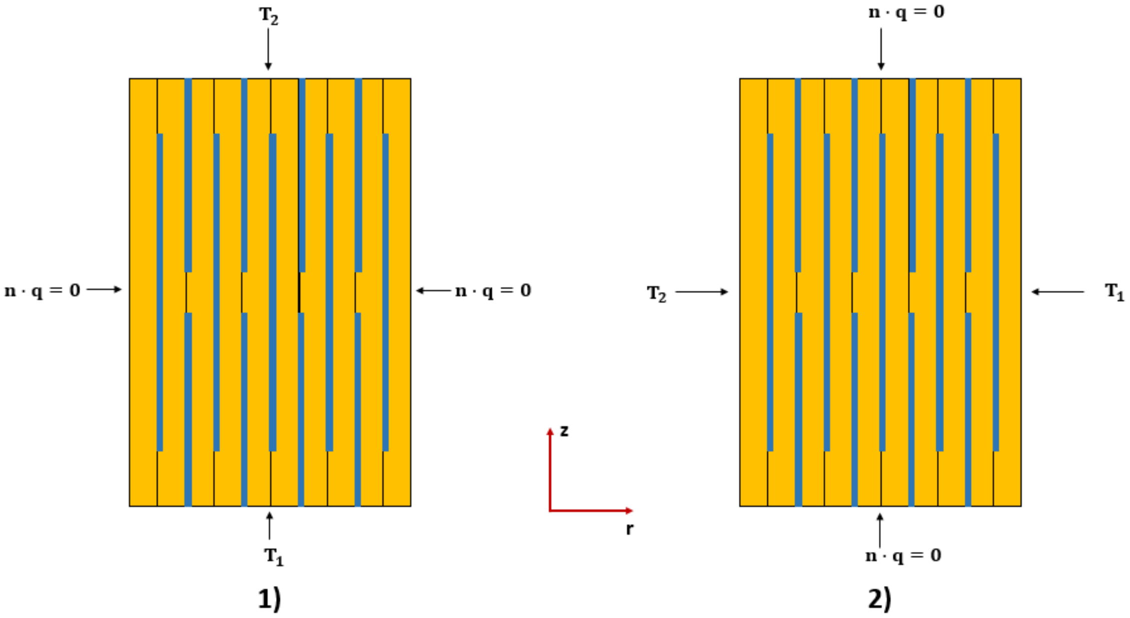

Figure 3.8: Illustration of the boundary conditions for the thermal simulations when a temperature difference is applied in z-direction (1) and in r-direction (2). Yellow is PP and blue is metal.

3.5 Large Scale - Multiphysics Model

The geometry of the capacitor unit described in section 2.3 for electrical and thermal simulations in 3D space dimensions can be seen in Figure 3.9, the complete unit and the internal domain is displayed (2). On top of the elements there is a busbar-system to electrically connect the elements. The capacitor is displayed from above in Figure 3.10 (1) where the busbar-system is highlighted and the connection points (terminals) of the unit are seen (2). It can be observed that the upper (group 1) and lower (group 2) parts of the busbar-system have 3 terminals each. The geometry of one single element is shown in Figure 3.11, side view (1) and top view (2). It can be seen that the geometry consist of two domains, the dielectric and the bobbin. A number of simplifications have been made in the geometry,

- The bushings enclosing the terminal contacts have been left out to reduce mesh elements. The bushing material (epoxy) has a low thermal conductivity (in the range of $0,9\ W/mK$) and is close to insulation and therefore the boundary condition is set to thermal insulation.
- The busbar-system is placed in direct contact to the elements on the top and the bottom. For an actual unit there is a connection point between the zinc and busbar made by soldering.
- The zinc contacts have no thickness in the geometry to reduce mesh elements and the thickness is instead given as a parameter to a boundary condition.
- The case of the unit have no thickness in the geometry to reduce mesh elements and is instead given as a parameter to a boundary condition.

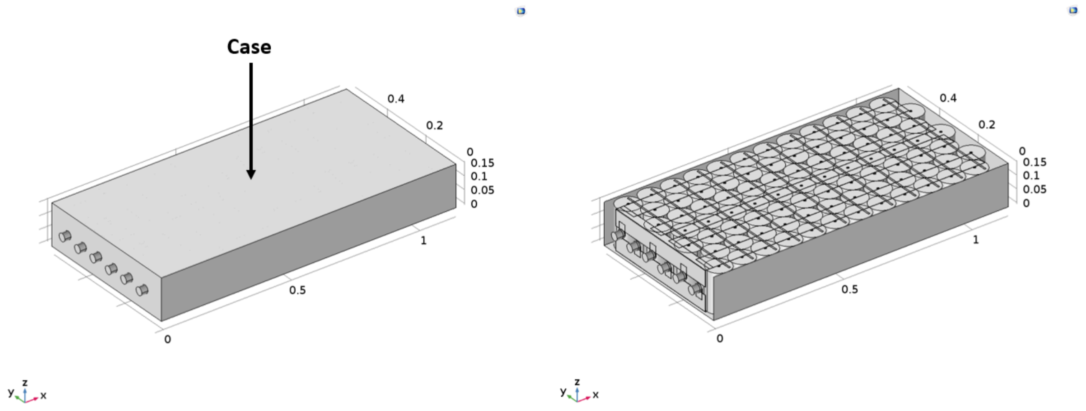

1) 2)

Figure 3.9: The complete geometry of the capacitor unit (1) and the geometry when the upper and front boundaries of the case are hidden to illustrate the inner domain (2). The grids are in m.

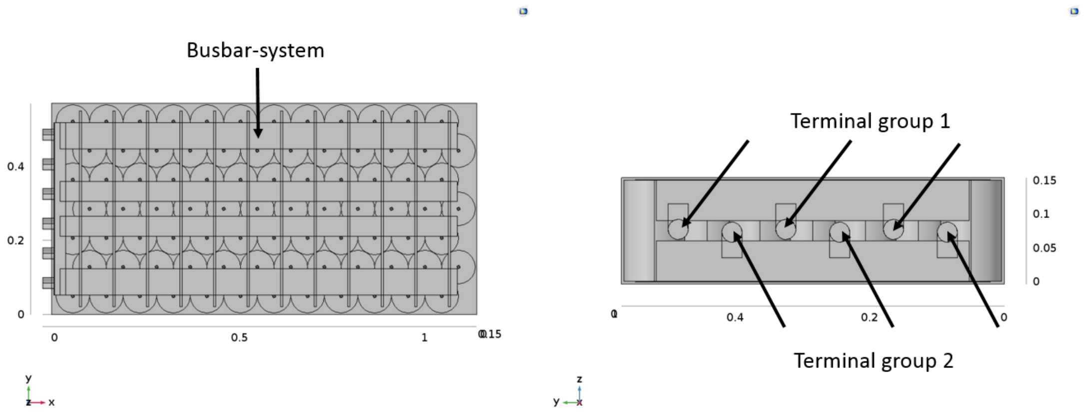

1) 2)

Figure 3.10: Top view of the geometry of the capacitor unit (1) and front view at the terminals (connection points) (2).The grids are in m.

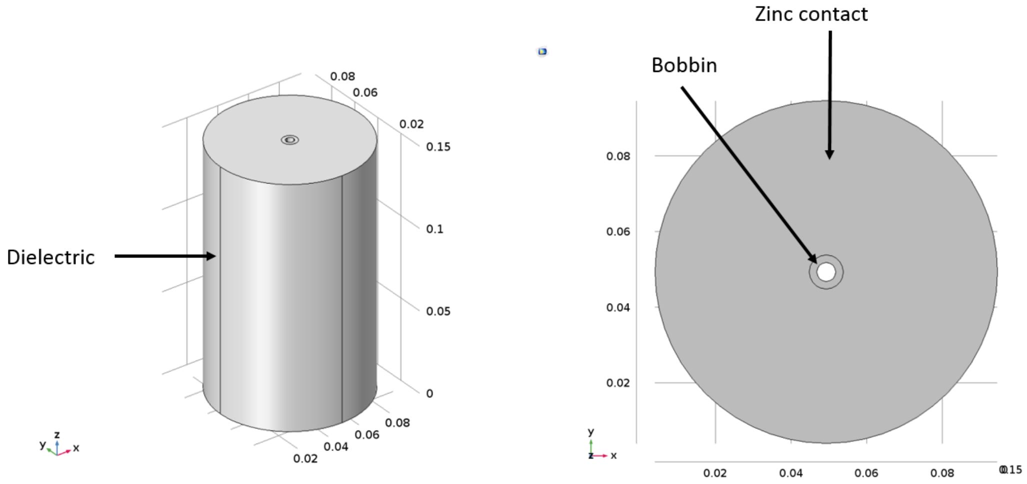

1) 2)

Figure 3.11: The geometry of one capacitor element (1) and a top view of the element (2). The grids are in m.

The dielectric of the elements are implemented by applying the effective properties computed on the small scale. A summary of materials of different domains and important properties are presented in Table 3.4. The important material properties for coupled electrical and thermal simulations are electrical and thermal conductivity. These two properties determines the losses in the busbar-system and temperature distribution for a stationary problem. The empty slots in the table is due to the domain is not solved for an interface where the property is used.

Table 3.4: Summary of the materials in the geometry and important properties [29].

Domain	**Material**	σ (S/m)	k (W/mK)
Busbar-system	Copper	5,998 10^7	400
Elements	Metallized films	effective properties	effective properties
Element contacts	Zinc	1,69 10^7	120
Terminals	Brass	1,54 10^7	79
Inside Case	PUR	-	0,2
Boundaries of case	Aluminum	-	238

3.5.1 Meshing of the Large Scale Model

The mesh applied to the entire geometry consist of tetrahedral elements which can be seen in Figure 3.12, complete mesh (1) and a zoom in at the corner of the of the unit with the upper case boundary hidden (2). Statistics of the mesh can be seen in Table 3.5 where it can be noted that the mesh for the large scale has a better quality than the mesh for the small scales.

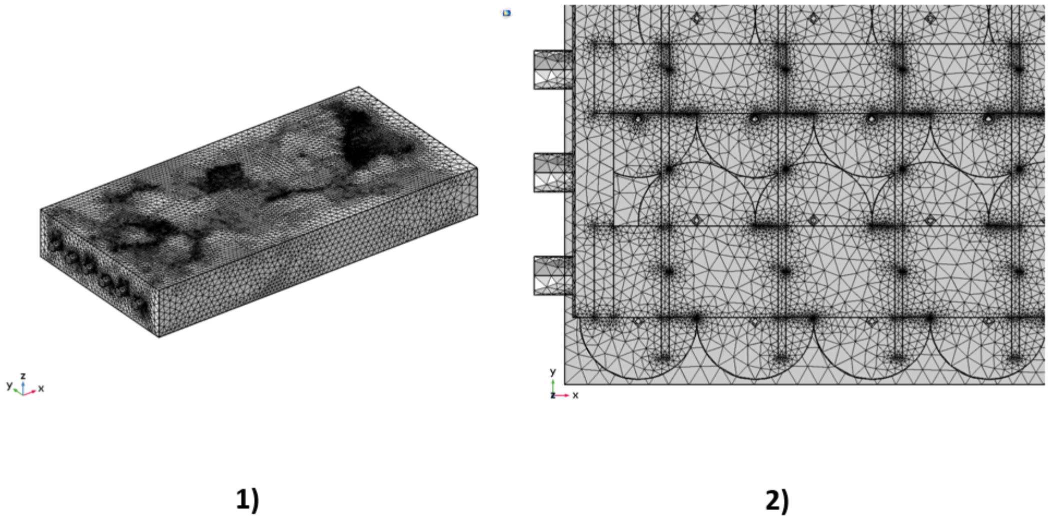

Figure 3.12: The mesh applied to the large scale geometry (1) and a zoom in of the mesh at the corner when the top case boundary is hidden (2).

Table 3.5: Summary of parameters and statistics of the mesh of the large scale model.

Element size parameters	
Max element size	176 *mm*
Min element size	32,8 *mm*
Max element growth rate	1,6
Curvature factor	0,7
Complete mesh statistics	
Number of elements	1172906
Min element quality	0,00043
Avg element quality	0,4992
Element volume ratio	$9{,}127{\cdot}10^{-10}$

3.5.2 Thermal Stability Test

Designs of capacitor units are evaluated by thermal stability tests according to IEC 61071 [30]. The test provides information about the thermal stability of the capacitor unit under overload conditions. The capacitor unit is inserted in an oven and preheated to + 5 $°C$ of the maximum specified operational temperature, in this case 66 $°C$. An illustration of the test setup can be seen in Figure 3.13, units in an oven (1) and the boundary conditions for the convection of the test unit (2). In this specific test, three units are placed in an oven with thermocouples placed at different points on the case. When all points have reached the desired temperature, a sinusoidal current of 50 Hz, 700 A rms, is applied for a period of at least 48 h. When the units have reached thermal steady state the test is finalized.

To reduce the required memory of the computational station, the test is simulated in stationary conditions and the computed result is compared with the steady state results from a test. As can be seen in (2), a fan is blowing air on the back of the unit and the air will circulate in the oven. It is forced convection in the oven but the speed of the fan is unknown and. The fan maintains the ambient temperature in the oven to 66 $°C$. The unit is placed on two planks of wood in approximately the middle of the oven together with two equal units. To reduce the complexity of the problem, the circulating air in the oven and the cooling of the unit is modelled as convective heat flux. The problem is then to determine the heat transfer coefficient which most likely will not be uniform for all sides. A first approximation is to assume the heat transfer to be uniform for the sides of the unit. Additionally it is assumed that the wooden planks does not affect the heat transfer much and can be neglected. The back of the unit will most likely be effected by the fan and have a higher heat transfer coefficient than the sides since this side is cooled by the fan. Furthermore, the front of the unit will not be affected by the fan in the same way but the cables connected to the terminals could cause external heating. Different parametric sweeps of the heat transfer coefficients at the sides, front and back are performed to validate the model and develop the best approximation. Additionally the element loss is uncertain since there is a deviation between computed and measured.

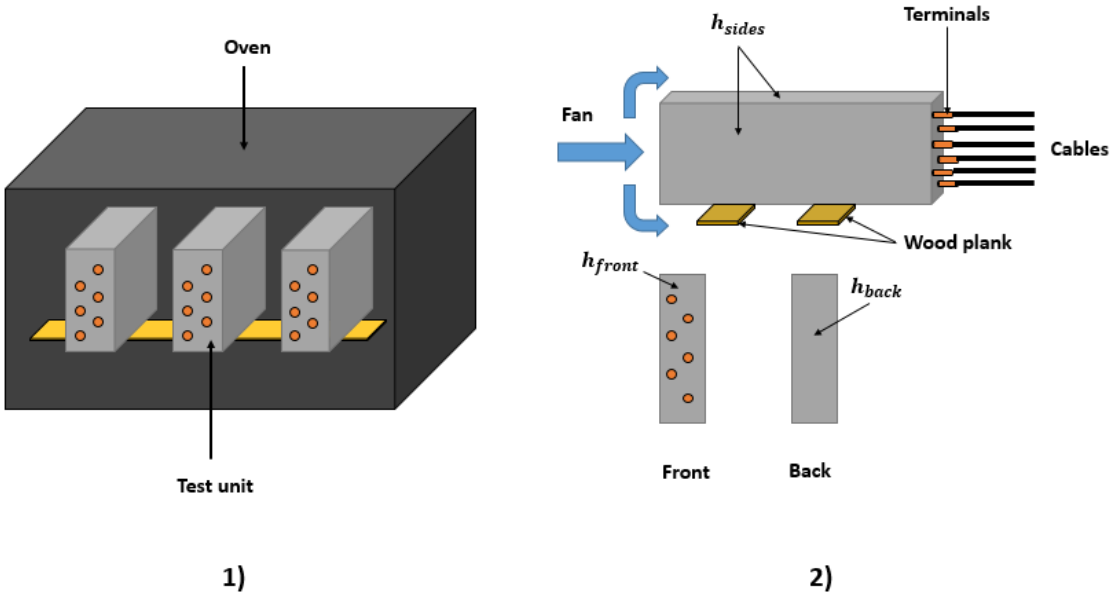

Figure 3.13: Illustration of the test setup for the thermal stability test (1) and the boundary conditions for the simulated unit (2).

3.5.3 Physical Interface and Boundary Conditions

The study of the large scale model consist of two interfaces solved in different study steps. First electric currents interface is solved in frequency domain and secondly heat transfer in solids is solved in stationary. The losses in the busbar-system and zinc contacts are added as heat sources to the heat transfer in solids by the nodes, electromagnetic heat source and boundary electromagnetic heat source. The electric currents interface is applied to the domains of busbar-system and elements. The boundary conditions and initial values implemented are as follows

1. Boundary Conditions
    - **Terminal-current**: $I_0 = \sqrt{2} \cdot 700\ sin(2\pi f)\ A$, applied to the 3 boundaries of terminal group 1. The frequency is 50 Hz.
    - **Ground**: Applied to the 3 boundaries of terminal group 2.
    - **Electrical Insulation**: applied to all exterior boundaries of the active domains

2. Initial Conditions
    - **Initial values**: 0 V applied to all domains.

The next step is the heat transfer in solids interface active on all domains in the geometry. The multiphysics nodes implemented to add the resistive losses in the busbar-system and zinc contacts as heat sources are electromagnetic heat source active on the domains of busbar-system and boundary electromagnetic heat source active on the horizontal boundaries of the elements. The interface is computed in stationary and boundary conditions and initial values implemented are as follows

1. Boundary Conditions
    - **Thin Layer case**: Material of aluminum with a thickness of $d_s = 2\ mm$ applied to exterior boundaries of the case.
    - **Thermal isolation**: Applied to the boundaries of the terminals outside the case.
    - **Heat Source**: One node applied to each element resulting in 84 nodes in total. Heat rate is set with $P_0 = tan(\delta) \cdot Q_{element}$, where $tan(\delta)$ is the computed losses on the small scale in $W/kvar$ and $Q_{element}$ is the reactive power produced by one element in var.
    - **Heat Flux**: Applied to the exterior boundaries of the case as convective heat flux with different heat transfer coefficient and an ambient temperature of $T_{amb} = 66{,}2\ °C$.

2. Initial Conditions
    - **Initial values**: 20 $°C$ applied to all domains.

Additionally the temperature dependence for the copper material in the busbar-system is also studied. A temperature dependent electrical conductivity of a material can be implemented in COMSOL by a linearized resisitvty as follows

$$\sigma = \frac{1}{\rho_0(1+\alpha(T-T_{ref}))} \tag{3.27}$$

where ρ_0 is the resistivty at the reference temperature in Ωm, α is the temperature coefficient for the material, T is the temperature in $°C$ and T_{ref} is the reference temperature of 20 $°C$ [22].

4

Simulation Results

In this chapter, the results obtained from simulations will be presented.

4.1 Small Scale Models

In this section results from the small scale electric and small scale thermal models will be presented.

4.1.1 Electrical Simulations

The computed potential distribution with the boundary conditions described in section 3.3.2 is shown in Figure 4.1, complete geometry (1) and zoom in at the central margin (2). It can be noted that the potential at the floating electrodes (Film B) and at the central margin are at half of the applied potential (green colour). Furthermore it can be seen that the top electrodes of Film A have a high potential and the opposite electrodes at the bottom have zero potential (grounded). This is expected since the metallic layers of Film A are in contact to the applied potential and ground. For the zoom in at the central margin, it can be seen that the electric field (red arrows) is perpendicular between the electrodes of Film A and Film B. For the upper part the electric field is directed from the electrode at high potential (Film A) towards the electrode at floating potential (Film B). For the lower part, the electric field is instead directed from the floating electrode towards the grounded electrode. Therefore, this arrangement results in two parallel-plate capacitors. One at the top, between the positive electrode (Film A) and the floating electrode (Film B) and one at the bottom between the floating electrode (Film B) and the grounded electrode (Film A).

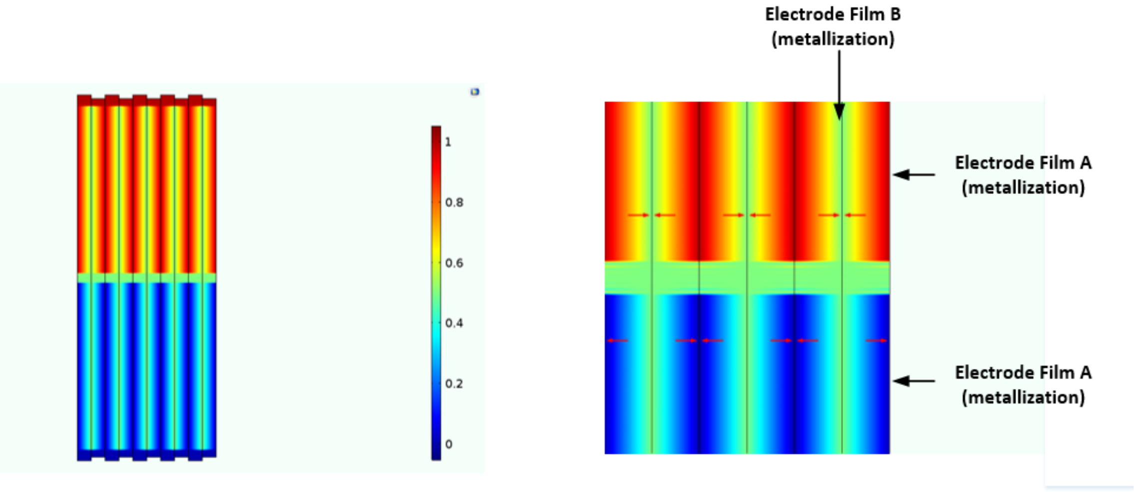

1)

2)

Figure 4.1: The electric potential distribution as surface plot for the entire geometry (1) and zoom in at the central margin with the electric field as arrow surface plot (2). The color bar is in V and the scale of the electric field arrows is $3 \cdot 10^{-5}$.

The current density will flow from the electrodes at high potential in the direction towards the central margin. The magnitude of the current density is at max close to the top and then decreases linearly to zero at the central margin. This can be seen in Figure 4.2, absolute value of the tangential current densities in the electrodes of Film A and Film B (1) and a sketch of the tangential and normal components (2). From Eq.3.11 it can be seen that the current densities consists of a resistive part and a capacitive part. The resistive part is a factor 10^4 smaller and that is why the absolute value is plotted. The current density at the top of Film A is constant at the heavy edge and gradually flows into the PP film to the electrode of Film B. The current density of Film B increases linearly due to more current from the electrode of Film A flows to it. At the central margin, the current density of Film B reaches a maximum and then starts to decrease linearly as current is flowing to the lower electrode of Film A. It can be seen from the sketch of the current density components for the electrodes of Film A that the current flows from the upper electrode of Film A to the electrode of Film B and then to the lower electrode of Film A. The current is thus flowing in Film A to Film B and then back to Film A.

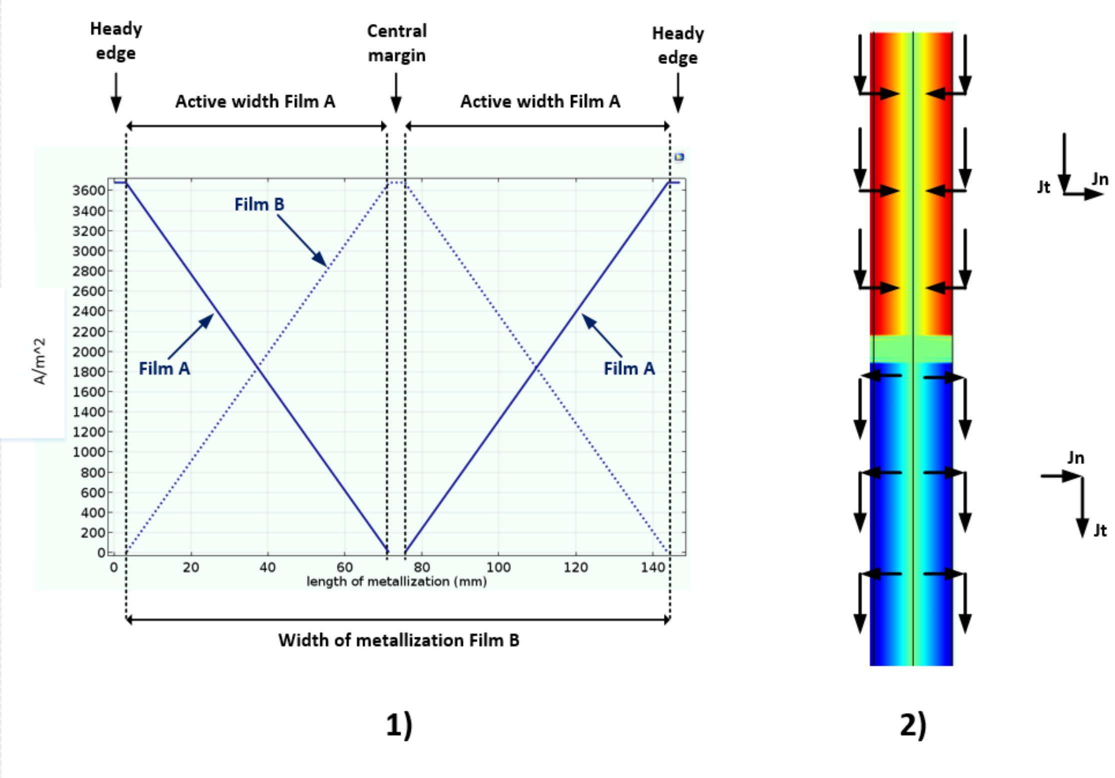

Figure 4.2: The absolute value of the tangential component of the current densities along the electrodes of Film A and Film B (1) and a sketch of the path of the current flow (2). J_t is the tangential component and J_n is the normal component of the current density.

The capacitance computed with the energy method from Eq. 2.6 can be compared to the capacitance calculated with the geometrical and material properties from Eq. 2.25. The results are presented in Table 4.1. It can be seen that the analytic result matches quite well with the computed with the energy method.

Table 4.1: Comparison of calculated and computed capacitance's on the small scale.

	Capacitance(F)
Analytic	$1,4654 \cdot 10^{-7}$
Energy	$1,47 \cdot 10^{-7}$

4.1.2 Evaluation of Resistive and Total Losses

The resistive losses on the small scale is computed by Eq. 2.28. Since the following parameters R_{sheet}, G_{factor} and $tan(\delta_0)$ varies between tolerances, the losses are evaluated at the min, max and a value in between. A summary of the results of the computations are presented in Table 4.2. The average resistive loss is 0,156 $W/kvar$ and the average total loss is 0,33 $W/kvar$. This value can be compared to the average measured value in production of 0,39 $W/kvar$. There is a deviation of 0,06 $W/kvar$. The measured loss is the total loss and the resistive part is unknown (can not be measured separately) and the dielectric part ($tan(\delta_0)$) is uncertain. It is difficult to measure the dielectric loss and the manufacture guarantee a $tan(\delta_0) <$ 0,2 $W/kvar$ but according to ABB it could be as low as 0,15 $W/kvar$. The measurement procedure may have an error due to the fact that the measured loss consist of contribution from the element as well as connection cables and so. The resistive loss vs frequency for the middle column can be seen in Figure 4.3. It can be seen that the edges has a small contribution to the total loss and the segmentation causes Film A to be the largest part of the total loss.

Table 4.2: Summary of loss evaluation, the different parameters are presented in their corresponding tolerance ranges.

Parameters	**Min**	**Avg**	**Max**
G$_{factor}$	2,8	3	3,2
R$_{sheet}(\Omega/square)$	9	11,25	15
$tan(\delta_0)$ $10^{-3}(W/kvar)$	0,15	0,175	0,2
Losses	**Min**	**Avg**	**Max**
Resistive(W/kvar)	0,114	0,148	0,2
$tan(\delta)$ $(W/kvar)$	0,26	0,32	0,41

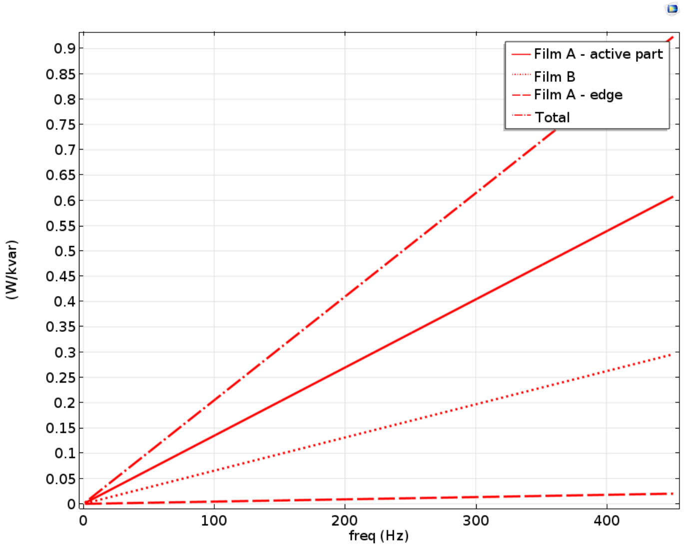

Figure 4.3: The different components of the resistive loss and the total resistive loss vs frequency.

4.1.3 Effective Electrical Properties

The effective conductivity and the effective relative permittivity of the small scale model are obtained by the averaging method described in section 3.1. Since the R_{sheet} and G_{factor} have tolerances, the effective properties are evaluated as the losses. A summary of the results of the computations are presented in Table 4.3. It can be seen that both the components of the effective permittivity are large. This is because the metallization gives rise to a large capacitance and the properties needs to account for this. In Figure 4.4, the average value of the effective properties are plotted vs frequency, the real part of the effective σ (1) and the effective ϵ' and ϵ'' are plotted in (2). It can be seen from the figures that the effective properties are constant in the range of 10^0 to 10^4 Hz. The capacitor unit in the large scale where the properties are to be used are only simulated for low frequencies i.e 50 Hz and therefore it is not of interest in this work what is happening for high frequencies. The imaginary part of the effective conductivity is not plotted since it has no real analogy to physics but is just a mathematical property.

Table 4.3: Summary of the computed effective electrical properties. The different parameters are presented in their corresponding tolerance ranges.

Parameters	**Min**	**Avg**	**Max**
G_{factor}	2,8	3	3,2
$R_{sheet}(\Omega/square)$	9	11,25	15
Effective properties	**Min**	**Avg**	**Max**
$Re(\sigma)$ (S/m)	$9{,}52\cdot10^{-5}$	$1{,}24\cdot10^{-4}$	$1{,}72\cdot10^{-4}$
ϵ'	$3{,}09\cdot10^{8}$	$3{,}09\cdot10^{8}$	$3{,}09\cdot10^{8}$
ϵ''	$3{,}42\cdot10^{4}$	$4{,}46\cdot10^{4}$	$6{,}20\cdot10^{4}$
Average properties	$Re(\sigma)=1{,}31\cdot10^{-5}$	$\epsilon'=3{,}09\cdot10^{8}$	$\epsilon''=4{,}69\cdot10^{4}$

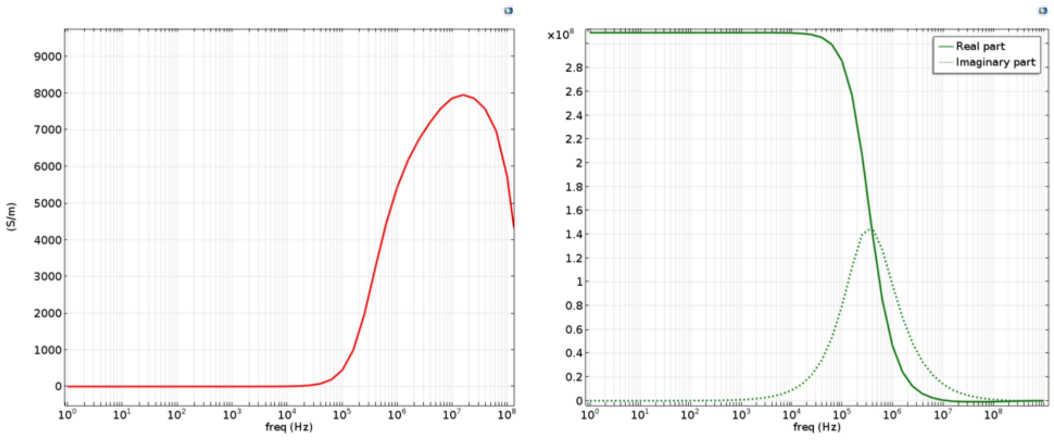

1)

2)

Figure 4.4: The effective electrical properties vs frequency. The real part of the effective sigma (1) and the real part and imaginary part of the effective epsilon (2). The x-axis are in log-scale.

4.1.4 Thermal Simulations

The results of the thermal simulations in the small scale are seen in Figure 4.5, where the temperature distribution and heat flux are plotted for a temperature difference in (1) r-direction and (2) z-direction are applied. It can be seen that a temperature difference in the r-direction gives rise to a heat flux in the same direction in (1) and the other way around in (2) when a temperature difference is applied in the z-direction.

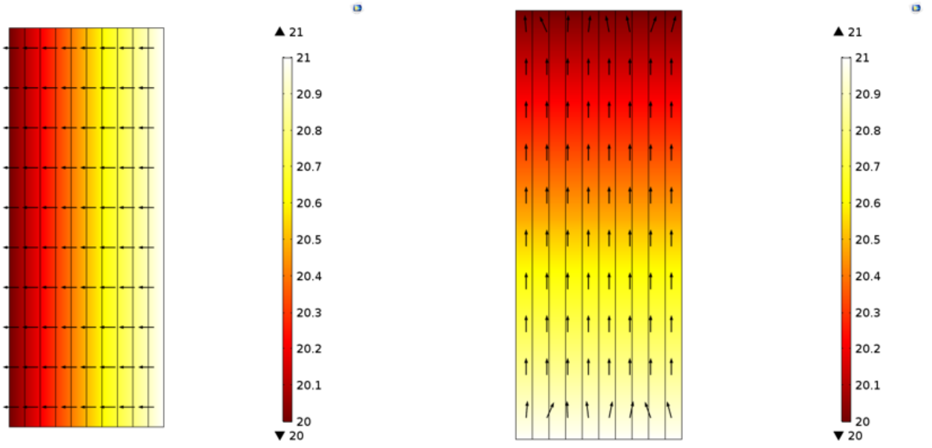

1)

2)

Figure 4.5: The temperature distribution as surface plot and the total heat flux as arrow surface for the temperature difference in r-direction (1) and z-direction (2). The color bars are in °C, the scale of the arrows are in (1) 0,0018 and (2) 5.

4.1.5 Effective Thermal Conductivity

Once the temperature distribution and total heat flux is obtained the effective thermal conductivity in the z-direction and r-direction are computed from Eq.3.8 and Eq.3.9. Since the thermal conductivity of PP is between 0,17-0,22W/mK, the effective property in both directions is evaluated for a minimum, maximum and a middle value of the conductivity of PP. The result are presented in Table 4.4. It can be seen that the conductivity in the r-direction is not affected by adding the metal but the conductivity in the z-direction is increased.The average value in the z-direction is $0,309$ W/mK. This value is close to $0,29$ W/mK which has been estimated by ABB Cooperate Research. When the metal layers are added to the PP film, the thermal conductivity increases despite the large difference in thickness.

Table 4.4: Summary of the computed effective thermal conductivities in the z and r-directions.

$k_{pp}(W/mK)$	$k_{metal}(W/mK)$	$k_z(W/mK)$	k_r (W/mK)
0,17	131,9	0,2768	0,17
0,195	131,9	0,309	0,195
0,22	131,9	0,341	0,22

4.2 Large Scale Models

A thermal stability test as described in section 3.5.2 is simulated in COMSOL multiphysic. The result is presented in different sections. Firstly the electric part and losses are presented, thereafter the boundary conditions for convective heat transfer, element losses and temperature dependent presented and finally the best approximation is chosen to present the thermal part of the results.

4.2.1 Electrical Part

The potential distribution together with the wave-forms of the input current and resulting voltage are shown in Figure 4.6. It can be seen that the potential distribution is uniform distributed on the top zinc contacts resulting in a parallel connection of all the elements. Furthermore the current and voltage wave-forms are pure sinusoidal where the voltage is lagging the current almost 90°. The terminal parameters and losses of the unit are presented in Table 4.5. It can be seen that the impedance of the unit has a resistive and capacitive part as expected. The resulting capacitance of one unit and one element can be compared to the rated capacitance of one unit of 9600 μF. The effective electric parameters corresponds well to the rated capacitance. The total computed loss of one unit is 0,496 $W/kvar$ which can be compared to the measured loss of 0,5 $W/kvar$. The deviation is 0,004 $W/kvar$ which corresponds to a deviation less than 1 %. If the measured loss of a element of 0,39 $W/kvar$ are used, the total loss will be 0,56 $W/kvar$. Either the loss in the busbar system is too high or the measured element loss is too high. The loss in the busbar-system is related to the current density and electric field. Since the impedance is correct, both the parameters are likely correct and the loss as well. As mentioned previously there is an uncertainty of the element loss measurement and this indicates that it could be an off-set.

Table 4.5: Summary of terminal parameters, capacitance's and losses of the model.

Terminal		**Losses**	
U (V)	0,106-j328	One element (W)	0,64
I (A)	989,95	All elements (W)	53,5
Z (Ω)	$1{,}056 \cdot 10^{-4} - j0,331$	Busbar-system (W)	20,9
$C_{element}$ (μF)	114,5	Zinc contacts (W)	5,98
C_{unit} (μF)	9616	One unit (W)	80,4
Q_{unit} ($kvar$)	162,2	One unit ($W/kvar$)	0,496

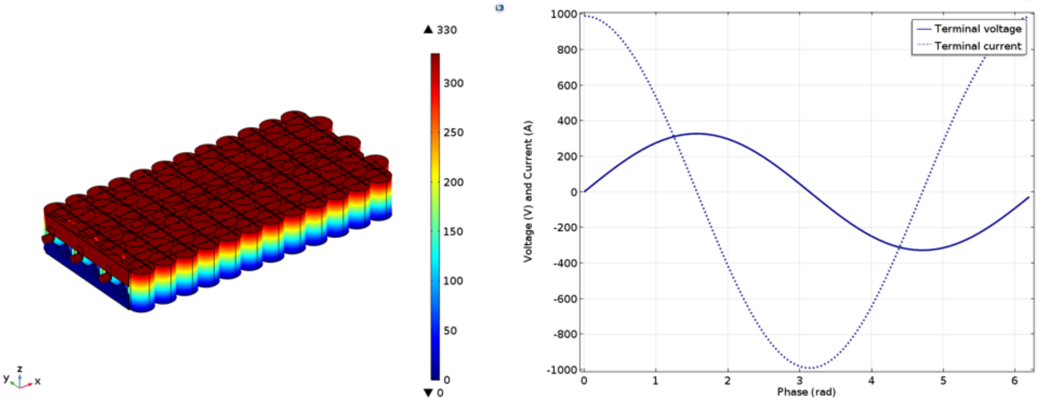

1) 2)

Figure 4.6: The potential distribution as surface plot (1) and the terminal current and voltage wave-forms for one period (2). The quantities are peak values and the colour bar is in V.

The current density in the busbar-system can be seen in Figure 4.7 as top view (1) and front view (2). The density will be higher in the third of the busbar-system close to the elements at the terminals. Additionally it can be seen from the front view, that the density have some spots of high density at the connection points. This distribution can be explained from the fact that all current is flowing in the busbar-system at the front and gradually as more current is flowing into the elements towards the back, the density is decreasing. The distribution of the current density will result in an uniform heating in the busbar-system.

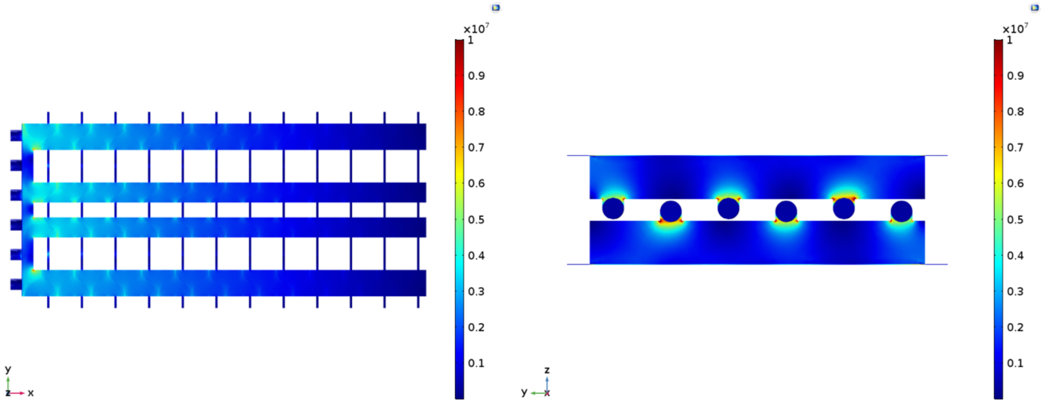

1) 2)

Figure 4.7: The current density as volume plot of the busbar-system, top view (1) and front view (2). The colour bar is in A/m^2.

4.2.2 Evaluation of the Simulation Setups

There is a number of uncertainties of the conditions in the oven when setting up a simulation of the thermal stability test. The heat transfer coefficient at the boundaries of the unit and the temperature dependence of the loss in the busbar-system are two major once. To evaluate the heat transfer coefficient to be used, firstly a parametric sweep is performed where the heat transfer coefficient is assumed to be uniform for all sides of the case. The heat transfer coefficient is swept in the range 10-20 W/m^2K. The resulting temperature at the measurement points can be seen in figure 4.8 where (1) the temperatures at the points for the test and different values of heat transfer coefficient are presented and in (2) the placement of the points are shown. It can be seen that the shape of the test curve is different to the simulated curves. The fan seems to cool down the back of the unit and point T_4 is close to ambient temperature at 66,2 $°C$. The heat transfer coefficient at the back should be higher than 20 W/m^2K to account for the effect and the back. The temperature decreases sharp after point T_2 in the test but for the simulated curves, the temperature starts to decreases sharply after point T_3. Point T_5 was not used in the test but for the simulation it provides information of the temperature distribution towards the back. The point T_0 which is not seen in the figure is placed at the front between the two middle terminals. The temperature at this point in the test is where the highest temperature is measured. For the simulations the temperature is instead highest at point T_2. To account for the effect at the front the heat transfer coefficient should be lower than 10 W/m^2K. It can be concluded from the shapes constructed of the points that in the simulations there is a hot spot located between T_1 and T_3. The temperature will then decrease at point T_4 and T_5 towards the back of the unit. In the test, the hot spot seems to be located at between T_0 and T_2 and the points T_4 and T_5 is at ambient temperature which may be due to the effect of the fan. The temperature rise at point T_0 compared to T_1 and T_2 may be due to external heating from the cables connected to the terminals.

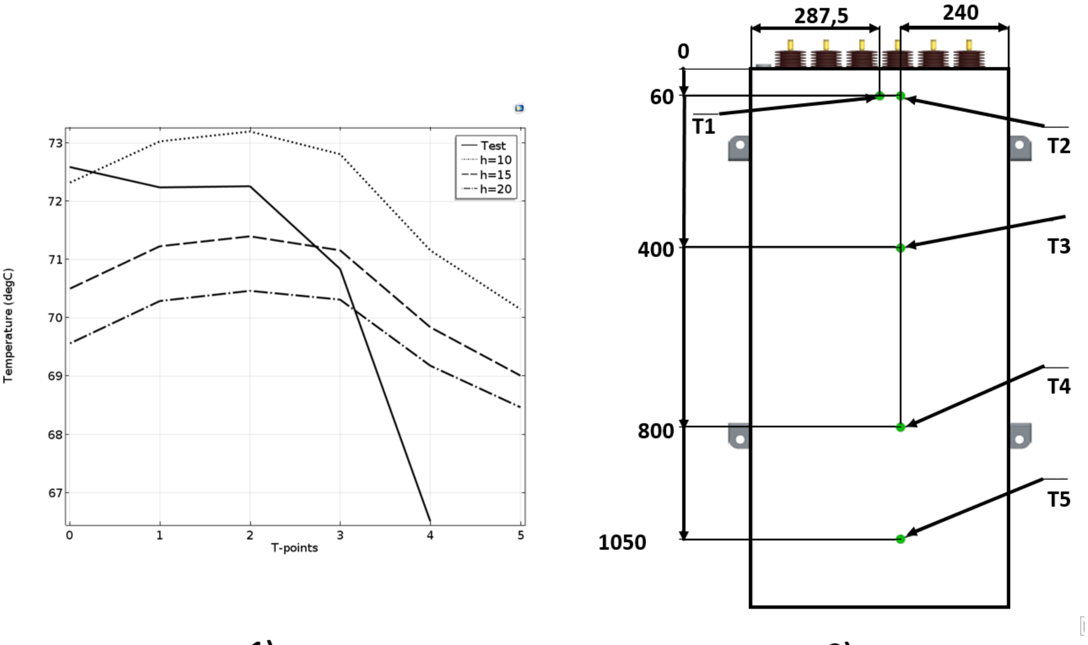

1) 2)

Figure 4.8: The temperature at different points on the case (1) and the location of the points on the case (2). The point T_0 is not seen in (2) but is placed in the middle of the case between two bushings. The dimensions are in mm

The loss in the busbar-system is dependent on temperature since the resistivty of copper increases with temperature and can be implemented in simulations by Eq.3.27. The effect of implementing the temperature dependence can be seen in Figure 4.9 (1). The temperature at the points T_0, T_1, T_2 and T_3 are increased which is reasonable since the current density is high in the area where the points are located. There is almost no losses occurring in the back of the busbar-system and then the effect of temperature is small but at the front this effect will be larger due to higher losses which can be seen in the figure. Still when this effect is accounted for the shape of the simulated curve deviates from the measured one. To approximate the measured values better, the heat transfer coefficient at the front is set to 5 and 10 W/m^2K while the heat transfer coefficient at the back is set to 100 W/m^2K. The resulting temperatures are plotted in Figure 4.9 (2). It can be seen that this pushes the temperatures at points T_0, T_1 and T_2 up while temperature at point T_5 is pushed down a little bit. The temperature at point T_2 for the simulation correspond well to the measured temperature at this point for this set of conditions. Even when the heat transfer coefficient is set to different values at the front, sides, back and the temperature effect on the loss in the busbar-system, there is deviation between the measured and simulated temperatures. Through a large value is set for the heat transfer coefficient at the back, there is a deviation at point T_4 of 3 $°C$. It can be concluded that the modelling of the heat transfer in the oven by convective heat transfer gives a rough approximation.

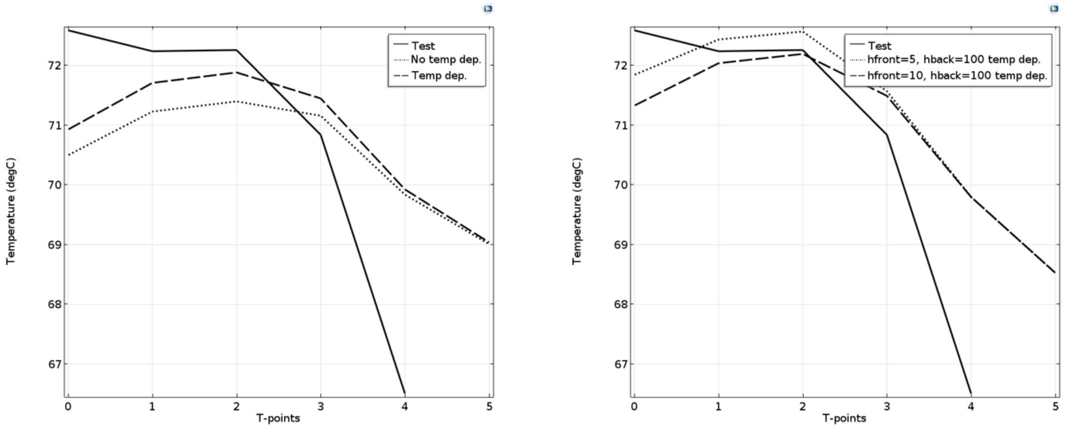

1) **2)**

Figure 4.9: The temperature at the points for no temperature dependence and for temperature dependence of the copper (busbar)(1) and the temperature at the points for different heat transfer coefficients at the front and rear boundaries of the case(2).

This is just one thermal stability test and the conditions for another test setup could be different. This is because the conditions are depending on a number of parameters. To simulate the heat transfer in the oven, more information is needed and it is not enough with just a few measurement points. But the evaluation is enough to develop a model that can be used for rough approximation of a thermal stability. This is good enough to estimate hot spots, average temperatures and max temperatures.

4.2.3 Thermal Part

To locate the hot spot and compute average and max temperatures, the evaluated conditions in section 4.2.2 are implemented. Temperature dependence of copper is implemented to the busbar-system, the following heat transfer coefficient are set $h_{front} = 10\ W/m^2K$, $h_{back} = 100\ W/m^2K$ and $h_{sides} = 15\ W/m^2K$. The computed temperature distribution of the unit can be seen in Figure 4.10, top view (1) and with the heat flux of the unit (2). The hot spot of the unit is located at the front close to the terminals and a bit into the unit. The hottest elements are located in this area and the coldest are the ones placed at the back. The hot spot corresponds to the area where the current density is high. This leads to a higher loss and and more heat generation and finally a hot spot. The temperature of the elements are dependent on the placement in the box. An element surrounded by other elements will almost only dissipate heat in z-direction, compared to the elements at the sides which can also dissipate heat in y and x directions. This can be seen in (2) where the z-component of the heat flux is dominating the y-components. These two effects and the placement affects the temperature of an element. In Figure 4.11 the temperature distribution and the heat flux of two elements are seen, an element placed in the hot spot (1) and an side element. It can be seen that the element in the hot spot is 5 °C hotter and the heat flux flowing towards the sides is negligible compared to the heat flux flowing upwards and downwards (z-direction). For the side element there is a more uniform distribution of heat flux.

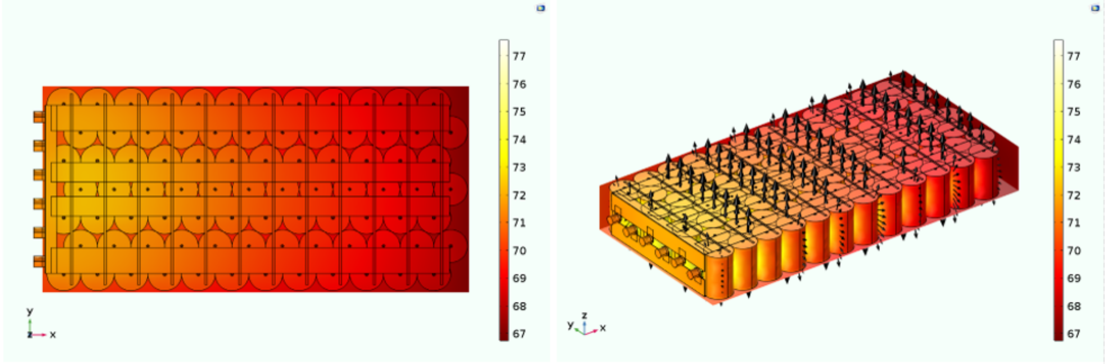

1) **2)**

Figure 4.10: The temperature distribution of the unit seen from above (1) and the temperature distribution and the heat flux of the unit (2). The colour bar is in °C.

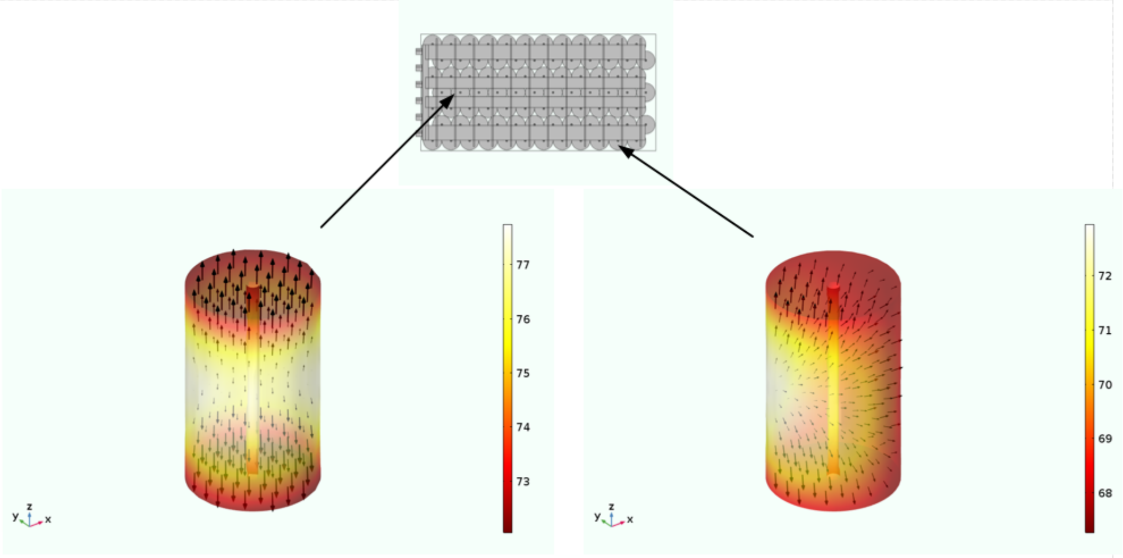

1) **2)**

Figure 4.11: The temperature and heat flux for one element located at the hot spot (1) and for one side element (2). The color bar is in °C.

The elements in the hot spot area are located in an area where more heat is generated due to higher losses in the busbar-system and therefore, exposed to an higher thermal stress. The hot spots of the elements in this area are located at the middle of the elements but this cannot be verified by the existing measurements. There is no possibility to verify the computed effective thermal conductivity of the metallized PP film at this point. Because no measurement points was placed inside the bobbins during the test used for comparison. As mentioned the maximum temperature will be at the center of the elements in the hot spot area and the maximum temperature of the busbar-system will also be located in the same area. The maximum and average temperatures of the unit and different domains are computed and summarized in Table 4.6. It can be seen that the maximum temperature of the unit is the same as for the elements placed in the hot spot. The average temperature of the unit is 72,9 $°C$ which is an average temperature rise of 6,7 $°C$ compared to the ambient temperature. The rear side of the unit has the lowest average temperature about equal to the ambient temperature which is expected since the heat transfer coefficient is very high there. The busbar-system has an average temperature of 70,8 $°C$ and a difference of 1,6 $°C$ between the maximum and average temperatures. As with the computed maximum temperature of the element placed in the hot spot, it is not possible to evaluate the maximum temperature of the busbar-system since no measurement points were placed there.

Table 4.6: Summary of the maximum and average temperatures of the unit and different domains.

Domain	T_{max} $(°C)$	T_{avg} $(°C)$
Unit	77,75	72,87
Busbar-system	72,41	70,82
Terminals	71,61	71,4
Elements	77,75	73,34
Aluminum Case		
Front	71,52	70,9
Rear	67,1	66,86
Upside and downside	71,04	69,28
Sides	70,16	68,79

5

Conclusion

In this study, the model of a capacitor unit for HVDC Light applications has been developed and simulations of a thermal stability test have been performed. The capacitor unit has been studied on different scales and by simulating a representative volume of the dielectric, effective electrical and thermal properties as well as losses have been computed. This study has shown that the impedance of a capacitor unit with the effective electrical properties applied to the elements, correspond well to the rated impedance of a unit. Additionally, the computed total loss of a unit deviates 1 % compared to the average measured loss. The computed average total loss on the small scale deviates 15 % compared to the averaged measured loss of a capacitor element. These findings suggests that the resistive loss may be overestimated and the total loss of an element may be lower than the measured loss. There are uncertainties regarding the measurement procedure and it should be evaluated and further measurements should be performed to eliminate errors. These findings suggest that in general, the multiscale modelling approach can be used to model capacitors with metallized film dielectrics, to overcome the difficulties of large difference in scales (dimensions).

The simulations and evaluations of a thermal stability test shows that an assumption of a uniform heat transfer coefficient in the oven is not valid. Simulations with different values of the heat transfer coefficient applied to different exterior boundaries of the case are a closer approximation of the heat transfer in the oven. Furthermore, temperature dependence of the conductivity of copper gives an even closer approximation. It is recommended that the simulations are compared against further thermal stability test since one test is not sufficient to validate the model. This study has identified a hot spot of the unit close to the terminals where the current density is high. The hot spots of the elements placed there are at the center of the elements. The elements at the sides and at the rear are less thermally stressed compared to the elements placed in the hot spot. The results shows that the difference of the maximum temperatures of the side elements and the elements in the hot spot, is close to 5-6 $°C$. The average temperature rise of the unit compared to the ambient temperature is 6,7 $°C$ and the average temperature of the unit is 72,9 $°C$.

5.1 Future Work

Further experimental investigations are needed to evaluate computed results and to provide a better understanding of the boundary conditions of a thermal stability test. It is suggested that at least one additional test is performed with a large number of thermocouples placed at different points of the unit, both inside and outside of the case. To estimate the heat transfer coefficient for different exterior boundaries of the case, several measurement points could be placed there. Additionally, points could be placed on the busbar-system to evaluate the temperature and hot spot. Finally points could be placed inside the bobbin of a number of elements to evaluate the temperature at the center.

Since the computed results suggest lower element losses than the averaged measured loss, future trials could be conducted to evaluate the impact of the equipment on the loss measurement. Furthermore, evaluation of the element loss could be done by calorimetric measurements. Individual measurement on elements to determine the thermal conductivity of the dielectric could also enhance the understanding and help to improve the model.

Bibliography

[1] C. Johnson. Numerical Solution of Partial Differential Equations by the Finite Element Method, Mineola, USA: Dover Publications, 2009.

[2] ABB "Introducing HVDC", 2015. [Online]. Available: http://www.abb.com/abblibrary/downloadcenter/. Accessed: June 1, 2017.

[3] O. Heyman. "HVDC Light - Proven technology in new applications| It's time to connect," ABB, 2013.

[4] ABB "DryDCap Enhancing eco-efficiency",2014. [Online]. Available: http://new.abb.com/high-voltage/capacitors/mv/capacitor-units/dc-dry-type-capacitors-drydcap. Accessed: May 4, 2017.

[5] R. W. Brown, "Distributed Circuit Modeling of Multilayer Capacitor Parameters Related to the Metal Film Layer," IEEE Transactions on Components and Packaging Technologies vol. 30, pp. 764-773, Dec. 2007.

[6] M. Makdessi, A. Sari and P. Venet., "Modeling of Metallized Polymer Films Capacitor's Impedance", in IECON 2012 - 38th Annual Conference on IEEE Industrial Electronics Society, pp. 4048-4053, Dec. 2012.

[7] H. Li, X. Huang, "Modeling of ESR in metallized film capacitors and its implication on pulse handling capability," Microelectronics Reliability vol. 55, pp. 1046-1053, April. 2015.

[8] F. Hedenus, M. Persson and F. Sprei, Sustainable Development: History, Definition the Role of the Engineer. 3 ed, Gothenburg, Sweden: Chalmers University of Technology, 2016

[9] IEEE,"IEEE Code of Ethics," IEEE.org, 2017[Online]. Available: http://www.ieee.org/about/corporate/governance/p7-8.html. Accessed 29 Mai, 2017.

[10] B. Jacobsson. "VSC-HVDC Transmission with Cascaded Two-Level Converters," Cigre B4-110, 2010.

[11] R. A. Hambley, Electrical Engineering: Principles and Applications. 6 ed, USA: Pearson, 2013

[12] D. Griffiths, Introduction to Electrodynamics, 2nd ed, Upper Saddler River, New Jersey, USA: Simon Schuster Company, 1989.

[13] D. Fleisch, A Student's Guide to Maxwell's Equations, Cambridge, UK: Cambridge University Press, 2008.

[14] L.D. Landau, Electrodynamics of continuous media, 2nd ed, Oxford, UK: Pergamon Press, 1984

[15] G. Raju, Dielectrics in Electric Fields, 2nd ed, Florida, USA: Taylor Francis CRC Press, 2017.

[16] A. K. Jonscher Dielectric Relaxation in Solids London:Chelsea Dielectric 1983.

[17] G. Picci and M. Rabuffi, "Status Quo and Future Prospects for Metallized Polypropylene Energy Storage Capacitors," IEEE Trans. Plasma Sci., vol. 30, pp. 1939-1942, Oct. 2002.

[18] D. Schroder, Semiconductor material and device characterization, 3ed, New Jersey, USA: Wiley - IEEE Press, 2006.

[19] X. Qi and S. Boggs, "Electrothermal failure of metallized film capacitor end connections - computation of temperature rise at connection spots," Journal of Applied Physics. Plasma Sci., vol. 94, pp. 4449-4456, Oct. 2003.

[20] C.W. Reed and S. W. Cichanowski, "The fundamental of ageing in HV polymer-film capacitors," IEEE Transactions on Dielectrics and Electrical Insulation, vol. 1, pp. 904-922, Oct. 1994.

[21] M.H El-Husseini, P.Venet, G. Rojat and C. Joubert, "Thermal Simulation for Geometric Optimization of Metallized Polypropylene Film Capacitors," IEEE Transactions on Industry Applications, vol. 38, pp. 713-718, Jun. 2002.

[22] COMSOL AB, AC/DC Module User's Guide Version COMSOL 5.2, 2015.

[23] S. Qin, J. Ho and M. Rabuffi. "Implications of the Anisotropic Thermal Conductivity of Capacitor Windings," IEEE Electrical Insulation Magazine, vol. 27, pp. 7-13, Jan. 2011.

[24] E.Tuncer, Y.V. Serdyuk and S. M. Gubanski, "Dielectric Mixtures: Electrical Properties and Modeling," IEEE Transactions on Dielectrics and Electrical Insulation vol. 9, pp. 809-828, Oct. 2002.

[25] B. Sareni, L. Krähenbühl and A. Beroual, "Complex effective permittivity of a lossy composite material," Journal of Applied Physics vol 80, pp. 4560-4565, Oct. 1996.

[26] F. Gori, S. Corasaniti, "Effective thermal conductivity of composites," International Journal of Heat and Mass Transfer vol 77, pp. 653-661, May. 2014.

[27] COMSOL AB, COMSOL Multiphysics Reference Manual Version COMSOL 5.2, 2016.

[28] COMSOL AB, Heat Transfer Module User's Guide Version COMSOL 5.2, 2015.

[29] C. Nordling and J. Osterman, Physics Handbook for Science and Engineering, 8ed, Lund, Sweden: Studentlitteratur AB, 2006.

[30] Capacitors for power electronics, IEC Standard 61071, 2007.